Petrophysical, geochemical, and hydrological evidence for extensive fracture-mediated fluid and heat transport in the Alpine Fault's hanging-wall damage zone

John Townend[1*], Rupert Sutherland[1,2], Virginia G. Toy[3], Mai-Linh Doan[4], Bernard Célérier[5], Cécile Massiot[1,2], Jamie Coussens[6], Tamara Jeppson[7], Lucie Janku-Capova[1], Léa Remaud[4], Phaedra Upton[2], Douglas R. Schmitt[8], Philippe Pezard[5], Jack Williams[3], Michael John Allen[9], Laura-May Baratin[1], Nicolas Barth[3,10], Leeza Becroft[3], Carolin M. Boese[1], Carolyn Boulton[1,9], Neil Broderick[11], Brett Carpenter[12], Calum J. Chamberlain[1], Alan Cooper[3], Ashley Coutts[13], Simon C. Cox[14], Lisa Craw[3], Jennifer D. Eccles[13], Dan Faulkner[9], Jason Grieve[3], Julia Grochowski[1], Anton Gulley[13], Arthur Hartog[15], Gilles Henry[5], Jamie Howarth[1,2], Katrina Jacobs[1], Naoki Kato[16], Steven Keys[1], Martina Kirilova[3], Yusuke Kometani[17], Rob Langridge[2], Weiren Lin[18,19], Tim Little[1], Adrienn Lukacs[3], Deirdre Mallyon[8], Elisabetta Mariani[9], Loren Mathewson[3], Ben Melosh[20], Catriona Menzies[6], Jo Moore[21], Luis Morales[22], Hiroshi Mori[23], André Niemeijer[24], Osamu Nishikawa[25], Olivier Nitsch[5], Jehanne Paris[5], David J. Prior[3], Katrina Sauer[3], Martha K. Savage[1], Anja Schleicher[26], Norio Shigematsu[27], Sam Taylor-Offord[1], Damon Teagle[6], Harold Tobin[7], Robert Valdez[28], Konrad Weaver[1], Thomas Wiersberg[26], Martin Zimmer[26]

[1]School of Geography, Environment and Earth Sciences, Victoria University of Wellington, PO Box 600, Wellington, New Zealand
[2]GNS Science, PO Box 30368, Lower Hutt 5040, New Zealand
[3]Department of Geology, University of Otago, PO Box 56, Dunedin 9054, New Zealand
[4]Université Grenoble-Alpes, Université Savoie Mont Blanc, CNRS, IRD, IFSTTAR, ISTerre, F-38000 Grenoble, France
[5]Géosciences Montpellier, Université de Montpellier, CNRS, Montpellier, France
[6]Department of Ocean & Earth Science, University of Southampton, Southampton SO14-3ZH, United Kingdom
[7]Department of Geoscience, University of Wisconsin-Madison, Madison, Wisconsin 53706, United States
[8]Department of Physics, University of Alberta, Edmonton, Alberta T6G 2R3, Canada
[9]School of Environmental Sciences, University of Liverpool, Liverpool L69 3GP, United Kingdom
[10]University of California, Riverside, California 92521, United States
[11]Department of Physics, University of Auckland, Private Bag 92019, Auckland 1142, New Zealand
[12]School of Geology and Geophysics, University of Oklahoma, Norman, Oklahoma 73019, United States
[13]School of Environment, University of Auckland, Private Bag 92019, Auckland 1142, New Zealand
[14]GNS Science, Private Bag 1930, Dunedin 9054, New Zealand
[15]Schlumberger Fiber-Optic Technology Centre, Romsey, Hampshire SO51 9DL, United Kingdom
[16]Department of Earth and Space Science, Osaka University, Osaka 565-0871, Japan
[17]Department of Geosphere Sciences, Yamaguchi University, Yamaguchi 753-8511, Japan
[18]Kochi Institute for Core Sample Research, Japan Agency for Marine-Earth Science and Technology, Kochi 783-8502, Japan
[19]Graduate School of Engineering, Kyoto University, Kyoto 615-8540, Japan
[20]Department of Earth and Planetary Sciences, McGill University, Montreal, Quebec H3A 0G4, Canada
[21]Curtin University, Perth, Western Australia
[22]ETH Zurich, Zurich, Switzerland
[23]Department of Geology, Shinshu University, Matsumoto, Asahi 3-1-1, Japan
[24]Faculty of Geosciences, HPT Laboratory, Utrecht University, 3584 CD, Utrecht, The Netherlands
[25]Department of Earth Science and Technology, Akita University, Akita City 010-8502, Japan
[26]GFZ German Research Centre for Geosciences, Telegrafenberg, 14473 Potsdam, Germany
[27]Geological Survey of Japan, AIST, Tsukuba, Japan
[28]Department of Geosciences, Pennsylvania State University, University Park, Pennsylvania 16802, United States

*Corresponding author: John Townend (john.townend@vuw.ac.nz)

Key points

- DFDP-2B data to 818 m true vertical depth reveal extensive fracturing of the Alpine Fault hanging-wall and high hydraulic conductivity
- The effective hydrogeological width of the damage zone exceeds the width implied by fracture density by at least an order of magnitude
- In areas of high relief and rapid slip, damage is controlled by coseismic, interseismic and inherited deformation modulated by topography

Abstract

Fault rock assemblages reflect interaction between deformation, stress, temperature, fluid, and chemical regimes on distinct spatial and temporal scales at various positions in the crust. Here, we interpret measurements made in the hanging-wall of the Alpine Fault during the second stage of the Deep Fault Drilling Project (DFDP-2). We present observational evidence for extensive fracturing and high hanging-wall hydraulic conductivity (~10^{-9} to 10^{-7} m/s, corresponding to permeability of ~10^{-16} to 10^{-14} m^2) extending several hundred meters from the fault's principal slip zone. Mud losses, gas chemistry anomalies, and petrophysical data indicate that a subset of fractures intersected by the borehole are capable of transmitting fluid volumes of several cubic meters on timescales of hours. DFDP-2 observations and other data suggest that this hydrogeologically active portion of the fault zone in the hanging-wall is several kilometers wide in the uppermost crust. This finding is consistent with numerical models of earthquake rupture and off-fault damage. We conclude that the mechanically and hydrogeologically active part of the Alpine Fault is a more dynamic and extensive feature than commonly described in models based on exhumed faults. We propose that the hydrogeologically active damage zone of the Alpine Fault and other large active faults in areas of high topographic relief can be subdivided into an inner zone in which damage is controlled principally by earthquake rupture processes and an outer zone in which damage reflects coseismic shaking, strain accumulation and release on interseismic timescales, and inherited fracturing related to exhumation.

1. Introduction

Active faults are geometrically and rheologically complex structures whose evolution and seismogenic behaviour are governed by processes acting on greatly varying spatial (<10^{-6} to 10^{6} m) and temporal scales (<10^{-3} to 10^{12} s) [e.g. *Tullis et al.*, 2007]. The characterisation of most faults typically requires the reconciliation of observations representing large spatial scales and short temporal scales (e.g. seismic tomography, earthquake seismology, and geodetic remote sensing) [e.g. *Bleibinhaus et al.*, 2007; *Fialko et al.*, 2002; *Zhang and Thurber*, 2003] or small spatial scales and long temporal scales (e.g. field and laboratory analysis) [e.g. *Caine et al.*, 1996; *Faulkner et al.*, 2010]. Moreover, many phenomena thought to affect fault behavior are macroscopically non-conservative (i.e. dissipative, such as friction) or non-linear (e.g. shear localisation and earthquake nucleation), or occur far from mechanical, thermal or chemical equilibrium (e.g. reactive fluid transport) [*Barber and Griffith*, 2017; *Hacker*, 1997; *Hobbs and Ord*, 2015; *Rice and Cocco*, 2007].

Describing the state of a fault at different points in its evolution or within a single earthquake cycle thus remains a first-order scientific challenge posing complex questions. In particular, how do heat and mass transport and fluid–rock interaction modify a fault zone during the earthquake cycle? Also, are the models of fault zone architecture derived from geological observations of inactive faults and geophysical measurements typically made of active faults compatible?

In this paper we present and interpret scientific drilling observations that constrain the hydraulic and thermal states of a major continental fault, the Alpine Fault, New Zealand, late in its typical interseismic phase. We focus in particular on direct petrophysical, hydrological, and geochemical evidence for high hydraulic conductivity in the hanging-wall, and discuss how this reflects the fault zone's structure and mechanical behavior at different points in the earthquake cycle.

The Alpine Fault in the western South Island of New Zealand (Figure 1) provides a globally rare opportunity to examine the conditions prevailing late in the typical interseismic cycle of an active plate boundary [*Sutherland et al.*, 2007; *Townend et al.*, 2009]. Paleoseismic evidence indicates that the central and southern portions of the fault [*Barth et al.*, 2013] have average recurrence intervals for M_W7+ earthquakes of less than 300 years, and the most recent large earthquake was 300 years ago in 1717 AD [*Berryman et al.*, 2012; *Cochran et al.*, 2017; *Howarth et al.*, 2012; 2014; *Howarth et al.*, 2016]. Scientific drilling has been conducted in two phases since 2011 under the auspices of the International Continental Scientific Drilling Program's Deep Fault Drilling Project (DFDP). The drilling has yielded rock and fluid samples and in situ geophysical measurements characterising the geological, geophysical, and geochemical structure of the fault zone and allowing the factors affecting the hydraulic and seismogenic behavior of the fault to be determined.

The first phase of DFDP drilling (DFDP-1) revealed a >6 order-of-magnitude decrease in permeability within ~30 m of the Alpine Fault's principal slip zone and a shallow hanging-wall geothermal gradient approximately four times that of the footwall [*Allen et al.*, 2017; *Carpenter et al.*, 2014; *Sutherland et al.*, 2012; *Townend et al.*, 2013; *Toy et al.*, 2015]. Subsequent pressure and temperature observations made in the Whataroa Valley during the second phase of the project, DFDP-2, revealed that the hanging-wall of the Alpine Fault has an extremely high geothermal gradient (~125°C/km) and is overpressured by ~10% with respect to a hydrostatic gradient [*Sutherland et al.*, 2017].

1.1 Seismotectonics and hydrogeology of the Alpine Fault

The Alpine Fault is the principal locus of motion between the Pacific and Australian plates in the central South Island, and has long been the focus of research into the structure and mechanics of continental faults [*Little et al.*, 2002a; *Norris and Cooper*, 2007; *Reid*, 1964; *Sibson et al.*, 1981]. The fault has slipped during the Late Quaternary at an average rate of 27±5 mm/yr horizontally and 6–9 mm/yr vertically [*Little et al.*, 2005; *Norris and Cooper*, 2001; 2007]. Uplift occurs most rapidly along the central section of the Alpine Fault, between the Wanganui and Karangarua rivers, resulting in a narrow, high-relief orogeny exposing amphibolite facies schist [*Koons*, 1987; *Little et al.*, 2005; *Vry et al.*, 2010].

The extent to which the Alpine Fault ruptures along its entire length or in characteristic segments remains a topic of active research [*Berryman et al.*, 2012; *Howarth et al.*, 2016]. However, the 300 year interval that has elapsed since the last known large (M_W7.9) Alpine Fault earthquake in 1717 AD exceeds both the most recent mean recurrence interval estimate of 291±23 years obtained for the southern on-land portion of the Alpine Fault [*Cochran et al.*, 2017] and the mean recurrence interval for the last four earthquakes inferred to have affected the central section of the fault [*Howarth et al.*, 2012; 2014]. In either case, the fault is now in the later stages of its inferred typical interseismic period, and the likelihood of a large (M_w7) or great (M_w8) earthquake occurring on the Alpine Fault within the next 50 years has been estimated to be ~27–29% [*Biasi et al.*, 2015; *Cochran et al.*, 2017].

At present, the plate boundary zone in the central South Island exhibits low levels of seismicity [*Boese et al.*, 2012; *Bourguignon et al.*, 2015; *Chamberlain et al.*, 2017; *Feenstra et al.*, 2016], sub-crustal seismicity [*Boese et al.*, 2013], tremor [*Wech et al.*, 2012; *Wech et al.*, 2013], and low-frequency earthquakes [*Chamberlain et al.*, 2014]. *Eccles et al.* [2015] recently reported observations of fault-zone-guided waves produced by earthquakes occurring close to or within the Alpine Fault, suggesting that the fault constitutes a single through-going structure to ~8 km depths. Using P- and S-wave earthquake tomography, *Guo et al.* [2017] showed that the fault is discernible seismologically to depths of 5–10 km.

Fluid flow within the uppermost 2–3 km of the Southern Alps orogen is dominated by the forced circulation of meteoric groundwater and produces hot springs in hanging-wall valleys [*Cox et al.*, 2015; *Reyes et al.*, 2010]. *Menzies et al.* [2014] analysed the stable isotope compositions of quartz, chlorite, and adularia sampled from veins in order to distinguish meteoric and metamorphic fluids and thereby determine the maximum depth of meteoric fluid circulation. Based on hydrogen isotopic ratios of δD=–84‰ to –52‰ the authors concluded that meteoric fluids circulate in the hanging-wall to depths exceeding ~6 km, near the base of the brittle–ductile transition zone, and suggested that these fluids are the principal mineralising fluids throughout the seismogenic crust. Analyses of strontium and helium isotopes [*Menzies et al.*, 2016] further indicate that the meteoric fluid-dominated flow regime is confined to depths of ~8 km in the hanging-wall by an impermeable Alpine Fault but that the fault nevertheless acts as a deep-rooted conduit for mantle-derived fluids.

1.2 The Deep Fault Drilling Project (DFDP)

Planning for a staged programme of scientific drilling targeting the central Alpine Fault began in 2009 [*Townend et al.*, 2009] and the first phase of the Deep Fault Drilling Project ("DFDP-1") commenced in 2011 at Gaunt Creek. During DFDP-1, two shallow boreholes were drilled through the hanging-wall mylonites and cataclasites, across the principal slip zone (PSZ), and into footwall gravels (DFDP-1A) and cataclasites [DFDP-1B; *Sutherland et al.*, 2011]. The fluid pressure measurements made in the DFDP-1B borehole show that the permeability of the hanging-wall decreases by approximately six orders of magnitude within approximately 30 m of the PSZ [*Sutherland et al.*, 2012] as a consequence of progressive alteration and mineralization associated with fluid flow along the fault [*Boulton et al.*, 2017b; *Boulton et al.*, 2014; *Schleicher et al.*, 2015; *Townend et al.*, 2013]. X-ray computed tomography images of fractures in the DFDP-1A and DFDP-1B cores shows that most detectable fractures are fully or partially filled by clay, quartz, or calcite [*Toy et al.*, 2015; *Williams et al.*, 2016].

A high temperature gradient of 62°C/km was measured in DFDP-1B [*Sutherland et al.*, 2012]. This value exceeds the regional footwall gradient by a factor of approximately 1.7 [*Townend*, 1999], and is consistent with the modelled effects of rock advection associated with uplift of the Southern Alps [*Allis and Shi*, 1995; *Koons*, 1987; *Koons et al.*, 1998; *Shi et al.*, 1996].

The second phase of the Deep Fault Drilling Project ("DFDP-2") was undertaken in the Whataroa Valley, approximately 7.5 km ENE from the DFDP-1 drill site, over a three month period in late 2014 (Figure 1). Two boreholes were drilled: the first, DFDP-2A, terminated within the sedimentary sequence and the second, DFDP-2B, reached a maximum measured depth (MD) of 893 m, corresponding to 818 m true vertical depth (TVD) once deviation is taken into account [*Sutherland et al.*, 2017; *Sutherland et al.*, 2015; *Toy et al.*, 2017].

2. Data acquisition and analysis

2.1 Borehole siting and technical operations

The Whataroa valley was originally identified as the optimal site for drilling to depths greater than 1 km on the basis of its location within the zone of most rapid hanging-wall uplift, the overall geometry of the Alpine Fault, and because existing roads provide access to the fault's hanging-wall [*Townend et al.*, 2009]. Subsequent active-source seismic studies suggested that the fault would be encountered at a depth of approximately 1100 m, and the drilling plan included provision for 200–300 m of footwall drilling.

The DFDP-2A borehole was spudded on 29 August 2014 and a dual-rotary drilling method was used to advance casing through the alluvial gravels and underlying Quaternary sequence. Due to the much greater than anticipated thickness of Quaternary sediments, DFDP-2A was terminated at 212.6 m and a second borehole (DFDP-2B) was spudded approximately 10 m away on 28 September 2014. This paper focuses exclusively on DFDP-2B unless otherwise noted.

DFDP-2B was drilled in two main stages (Figure 2). The uppermost sedimentary sequence was drilled using a combination of the dual-rotary method that advances casing at the same time as the hole is drilled, and conventional open-hole drilling. The first casing string (16") was advanced using the dual-rotary system to 76.8 m, the open hole was drilled to 197 m, and the second (14") casing string installed. The dual-rotary system was then used again to advance 12" casing to 236.6 m, and 10" casing into bedrock at 243.0 m. A 9.5" open hole was then drilled to 274.9 m and confirmed that bedrock had been reached. The second main stage of drilling, through the bedrock sequence, was undertaken using 8.5" bits to the final depth of 893.2 m (measured depth).

2.2 Cuttings analysis and lithologic interpretation

Cuttings samples were described and analyzed in hand specimen and thin section on-site throughout the drilling, providing near-real-time information about composition and structure of the drilled sequence [*Toy et al.*, 2017]. The sedimentary stratigraphy encountered in DFDP-2A consists (from top to bottom; Figure 2) of a young (<1–12 kyr) sequence of fluvio-glacial gravels (0–58 m sample depths) grading into sandy lake delta sediments (58–77 m), a thick sequence of lacustrine muds and silts containing rare diamictite (77–206 m; ~19 kyr), and a coarser till diamictite (below 206 m).

DFDP-2B intersected amphibolite facies schistose basement at 243 m depth (Figure 2). This lithology, known as the Alpine Schist, is part of the Aspiring Lithologic Association subdivision of the Torlesse Supergroup [*Cox and Barrell*, 2007; *Toy et al.*, 2017]. The non-mylonitic Alpine Schist is an L-S tectonite with a centimeter- to decimeter-spaced planar or crenulated foliation of quartz-feldspar and mica layers, and distinct quartz rod lineations pitching southwest and rarely containing both synthetic and antithetic shear bands with a distinct quartz lineation pitching steeply southwest [*Little et al.*, 2002a; b; *Toy et al.*, 2015]. Within the Alpine Fault zone, the schist fabric is progressively reworked. The smallest ductile shear strains have generated protomylonites, which have millimeter- to centimeter-spaced foliations that are alternately rich in quartz-feldspar and mica ± amphibole. These may retain isoclinal fold hinges formed during deformation of the precursor Alpine Schist [*Little et al.*, 2002b; *Toy et al.*, 2012] and are distinctly transected by extensional shear bands spaced at 5–15 mm [*Gillam et al.*, 2014], with synthetic sense to the Alpine Fault. Progressively higher strains have resulted in mylonites with S-dominated fabrics of millimeter-spaced quartz-feldspar and mica and <5 mm-spaced shear bands. Within a few hundred meters of the PSZ, ultramylonites lack a spaced foliation and shear bands can only be observed microscopically.

The lithologies of DFDP-2B cuttings could not generally be differentiated based on macrostructural features, due to the cuttings' small sizes [*Toy et al.*, 2017]. However, certain microstructural features were found to be useful indicators of mylonitic ductile deformation, allowing correlation to position within the ductile fault rock sequence known from outcrops and described above. As drilling progressed, signs of increasing ductile shear strain were observed, including a progressive reduction in the mean grainsize of quartz (>100 μm in schists and protomylonite, and <100 μm in mylonites), an increase in the maximum grainsize of mica (from 10–100 μm in non-mylonitic Alpine Schist to a few millimetres in protomylonites and mylonites), the appearance of asymmetric shear bands (indicative of protomylonite or mylonite in outcrop samples), and changes in the microstructural arrangement of accessary phases [*Toy et al.*, 2017].

The identification of the transition from protomylonite to mylonite at 830 m measured depth informed the decision to case the borehole in preparation for the switch from rotary drilling to wireline coring. During the casing operation, the casing string parted due to an idiopathic metallurgical failure that was not noticed until after the casing had been cemented. The consequence of this was that the borehole was inaccessible below 436 m, and the decision was made to re-cement the upper casing string and annulus, and drill out the cement to 400 m. In other words, DFDP-2B is currently accessible to 400 m via 127-mm internal diameter casing. An armored optical fiber cable installed during the casing procedure extends to the total drilled depth of 893 m and has since been used to acquire temperature and optical seismic data (Figure 2) [*Sutherland et al.*, 2017].

2.3 Wireline logging measurements

Full details of the DFDP-2 wireline logging program were described by *Sutherland et al.* [2015]. In total, 16 logging tools were deployed, many in a stacked configuration that enabled multiple tools to be run simultaneously. Due in part to technical problems that caused delays in drilling, it was possible to re-log several intervals of the borehole on multiple occasions and thus to acquire data at different points in the borehole's thermal and hydrologic equilibration. A total of 19 km of wireline data was collected from DFDP-2B during 52 runs (separate insertions of logging tools) made over 18 logging sessions. Acoustic borehole televiewer (BHTV) data spanning 4.8 km were collected, providing rare acoustic imagery of metamorphic fault rock structures.

Following the completion of drilling, the wireline logs were depth-matched and aligned to a common datum using cross-correlation of the natural gamma and resistivity logs and a linear depth-dependent adjustment to compensate for wireline stretching [*Remaud*, 2015]. The logs are presented here with respect to measured depth, although reference is made to true vertical depth which takes into consideration the borehole's deviation where appropriate (Supporting Information Figure S1).

In this paper we examine variations in natural gamma, deep and shallow resistivity, sonic velocity and the BHTV imagery. Natural gamma, a measure of the natural radioactivity of the rock mass, was recorded in DFDP-2B on both total gamma and spectral gamma tools [*Ellis et al.*, 2007], but the spectral measurements (which enable the contributions of the key radioactive elements ^{40}K, ^{232}Th, and ^{235,238}U to be distinguished) yielded very low counts and are not presented in this paper. We measured resistivity using dual laterolog tools that yield measurements obtained with different sensor spacings: the shallow resistivity measurements are sensitive to interaction of conductive drilling mud with fractures, whereas the deep resistivity measurements are diagnostic of the rock mass itself. The ratio of deep to shallow resistivity is sensitive to both fluid invasion and formation anisotropy [*Ellis et al.*, 2007; *Pezard and Anderson*, 1990].

2.4 Mud property measurements and hydraulic tests

Fluid levels were maintained within the borehole during drilling by pumping and circulating mud, and this process perturbed fluid pressures in the surrounding rock mass. When drilling and mud circulation ceases, fluid flows into or out of the borehole as fluid pressures equilibrate: this process can be used to measure the bulk permeability of the rock mass and the equilibrium fluid pressures. We performed 33 such tests at eight depths by measuring mud levels in the open borehole after circulation had stopped for intervals of ~0.5–167 hours, using a measuring tape and water level sensor [*Sutherland et al.*, 2017; *Sutherland et al.*, 2015].

We refer to repeated mud level measurements during breaks in circulation as "slug tests" [e.g. *Bouwer and Rice*, 1976; *Papadopulos et al.*, 1973]. This usage is not strictly appropriate as the induced changes in head are not instantaneous and the durations of the measurements are short relative to the estimated equilibration times. We describe the slug test responses using a function of the form $m(t) = a + b\exp(-t/c)$, where $m(t)$ is the mud level at time t relative to a datum at the top of the borehole, c is a characteristic equilibration time related to the hydraulic conductivity of the rock mass adjacent to the borehole, and a and b are constants related to the initial and fully equilibrated mud levels.

We obtain an order-of-magnitude estimate of hydraulic conductivity using the *Hvorslev* [1951] method, whereby $K \sim r_e^2 \ln(R_e/r_w)/2Lc$. Here r_e is the borehole radius in the open-hole section (8.5" borehole), r_w is the radius in the measurement interval (10" casing), R_e is the effective radius of fluid dissipation (assumed to be 0.1–1 m on the basis of the deep resistivity measurements), L is the length of open-hole (of order 100 m), and c is the characteristic equilibration time.

In addition to the mud level data reported here, a combination of automated and manual measurement techniques were used to record the physical properties of drilling mud entering and leaving the borehole throughout the operational phase. The volume of mud entering and leaving the borehole was monitored intermittently during circulation by measuring the height of mud in the suction (inflow), returns, and outflow pits, using a graduated scale. Continuous measurements of the mud level in the suction pit were made using a vibrating wire piezometer connected to a data logger [*Sutherland et al.*, 2015].

2.5 Geochemical monitoring

A systematic real-time analysis of the composition of gases extracted from drilling mud was undertaken while drilling DFDP-2B using methodology described by *Erzinger et al.* [2006]. A gas–water separator was used to extract gas from mud flowing out of the borehole. Major and trace element concentrations were determined in the field with a quadrupole mass spectrometer, light hydrocarbons with a gas chromatograph equipped with a flame ionization detector, and radon (Rn) with a Lucas cell. Measurements of H_2, He, N_2, O_2, CH_4, CO_2, and Ar were made at 1 minute intervals with the mass spectrometer; measurements of CH_4, C_2H_4, C_2H_6, C_3H_6, C_3H_8, i-C_4H_{10}, and n-C_4H_{10} were made at 10 minute intervals with the gas chromatograph; and Rn was measured at 1 minute intervals.

3. Results

3.1 Borehole geometry and shape

At depths below ~300 m, DFDP-2B was observed in successive BHTV runs to be deviating towards the northwest as measured by the inclinometer and magnetometers on-board the televiewer (Figure 3). A maximum deviation from vertical of 44° towards an azimuth of 340° geographic (318° magnetic) was reached. The amount of deviation increases approximately linearly with depth below 300 m (at ~0.1°/m), despite the use of seven different BHA configurations and drill bits that yielded markedly different rates of penetration (Figure 3).

As described in further detail below, analysis of fractures and foliation planes identified in the BHTV logs below 264 m (i.e. in the basement rocks) reveals that both sets of features predominantly dip 50–60° towards the southeast, consistent with regional mapping [*Cox and Barrell*, 2007]. This indicates that the borehole deviated towards the average up-dip direction, or slightly (10–30°) northward (clockwise) of that direction. The slight difference in deviation direction from the foliation's up-dip direction is likely a consequence of the clockwise rotation of the drill bit.

The large deviation of the DFDP-2B borehole prevented the arms of the mechanical caliper from opening correctly, resulting in the caliper measurements being systematically lower than the actual borehole radius. To obtain more reliable estimates of the borehole radius along the borehole's full length, we fitted a circle to the acoustic returns from the borehole wall at each sampling depth and converted travel time to equivalent radius using a temperature- and pressure-dependent relationship [*Massiot*, 2017].

BHTV images show that the borehole retained an approximately circular cross-section over its entire length, despite the deviation. Above ~480 m, the imagery shows asymmetric amplitudes inferred to indicate that the tool was resting against one side of the borehole due to the mechanical effects of drilling and BHA wear. No evidence for borehole breakouts or tensile cracks was observed.

3.2 Petrophysical observations

The logs exhibit the following key petrophysical features (Figure 3), which are discussed in further detail below:

1. Natural gamma logs display high frequency oscillations, with values varying between approximately 100 and 180 API and increasing weakly but systematically with depth at a rate of ~0.02 API/m. The character of the gamma log changes at approximately 470 m MD, with an increase in the wavelength of oscillations, and an increase in the amplitude of short-wavelength (meter-scale) anomalies.
2. Shallow and deep resistivity also exhibit modest but systematic increases with depth, although there is a zone of uniformly low values between 320 m and 470 m. Below 400 m MD, both resistivity parameters increase systematically with depth, reaching maximum values of 700 Ω·m (deep) and 440 Ω·m (shallow).
3. The sonic waveform data exhibit a systematic increase in amplitude with depth, which may reflect increased fracture density and scattering. The derived Vs curve is centered on a mean value of ~2300 m/s below approximately 550 m depth, and shows no particular trend with depth.

Despite the rather monotonous lithology revealed on-site by cuttings analysis, the geophysical logs can be visually sub-divided into several semi-quantitative petrofacies that describe different depth intervals. Above 320 m, gamma, resistivity, and BHTV amplitude are high and sonic amplitude is low. Between 320 m and 468 m, gamma, resistivity and BHTV amplitude are lower. There are pronounced changes in several of the logs at ~468 m depth, notably increases in gamma, sonic amplitude, and BHTV amplitude, and a decrease in deep/shallow resistivity. These changes do not correspond to an identified lithologic change or to a change in bit. Below this depth, the ratio of predominantly micaceous cuttings to predominantly quartz+feldspar cuttings increased gradually, and mica fish and striations on generally micaceous surfaces were both detected [*Toy et al.*, 2017]. Variations in mechanical wearing and winnowing associated with changes in the rates of drilling and mud circulation, and sample washing, may have affected sampling of the micaceous cuttings. However, the overall increase in gamma within increasing depth is consistent with a higher proportion of potassium-bearing minerals, such as muscovite or biotite.

Between 508 m and 706 m (along the borehole), an interval spanning three different bit and BHA configurations, gamma and sonic amplitude are both high. Deep and shallow resistivity, the deep/shallow ratio, and sonic amplitude all decrease abruptly at 706 m, marking the top of an approximately 30 m-long interval. *Toy et al.* [2017] recognized a compositional change in the cuttings at approximately 700–720 m but this is less distinct than the changes seen in the wireline data. At approximately 736 m, the resistivity parameters all increase abruptly: this depth also coincides with a pronounced reduction in geothermal gradient but does not otherwise correspond to distinctive changes in the other logging parameters. At 794 m, gamma, resistivity, and sonic amplitude all increase and remain high until 883 m, below which they are low until the base of the borehole at 893 m.

Resistivity and gamma logs spanning the entire logged interval of DFDP-2B (Figure 4) demonstrate the consistency of repeated logs and similarities between the two parameters that are most likely governed by variations in lithology. The raw gamma data exhibit high-frequency variations typical of finely layered formations. We apply a median filter spanning a 2.5 m-long (50 sample) running interval to emphasize long-wavelength features likely associated with lithology rather than fracturing or other structural features. After filtering, the downward increases in the composite gamma (Figure 4b) and resistivity logs (Figure 4c) are evident, with gradients of 0.02 API/m and 0.35 Ω·m/m, respectively. Both gradients are substantially lower than the corresponding values measured in hanging-wall ultramylonites and cataclasites within 70 m of the PSZ in the DFDP-1B borehole (~1.3 API/m and ~3.6 Ω·m/m, respectively), and the resistivity gradient is of the opposite polarity [*Townend et al.*, 2013]. We discuss the implications of this in Section 4.

A 26 m-long interval of the borehole is illustrated in Figure 5 to highlight several features of the dataset produced by planar structures intersecting the borehole and visible in the BHTV imagery as sinusoids. These structures are in some cases associated with borehole enlargement, visible in the BHTV caliper log, distinctive zones of low deep/shallow resistivity (due to the infiltration of low-resistivity mud), strong attenuation and/or scattering of the sonic waveforms, and are presumed to be either foliation or fractures. Not all the structural features are large enough or sufficiently well-imaged to have distinctive electrical or sonic manifestations. In this paper and as a first approximation, we treat as fractures only those features visible in both the BHTV amplitude and travel-time logs; in other words, those features that exhibit an impedance contrast with the adjacent rock and are associated with borehole enlargement. Figure 5 also illustrates the very high degree of repeatability of successive electrical logs, which exhibit wiggle-for-wiggle agreement at the scales logged.

The structural observations made using BHTV logs are summarized in Figure 6. In total, 2242 features were identified and their geometries determined [*Massiot*, 2017]. Of these, 1566 (69.9%) are interpreted to represent fractures, based on the criterion described above, with the remaining 676 (30.1%) structures representing foliation not associated with borehole enlargement or other petrophysical signals. After correction for sampling bias related to the borehole's orientation, the average (Fisher) pole of the fractures has an orientation of 327/36 (trend/plunge) corresponding to an average plane striking 057° and dipping southeastward at 54°, and the average pole of the foliation is 323/34, corresponding to a plane striking 053° and dipping southeastward at 56°. In other words, the inferred fractures are subparallel to the foliation, and both are of similar orientation to the foliation observed in outcrop. Similar foliation-parallel fractures were observed in cores from the Amethyst Tunnel [*Williams et al.*, 2017b].

3.3 Temperature measurements

Temperature measurements made in DFDP-2B during wireline logging runs revealed substantially higher temperatures than anticipated on the basis of the 62±2°C/km geothermal gradient measured previously in the nearby DFDP-1B borehole (Figure 7). The maximum temperature recorded in DFDP-2B during drilling operations was 83.7°C at 817.95 m depth (TVD). Subsequent equilibration of the borehole measured by distributed temperature sensing methods resulted in an equilibrium temperature at the bottom of the borehole of 110°C, and the drilled interval as a whole has a geotherm of 125±55°C/km [*Sutherland et al.*, 2017].

The most distinctive change in geotherm occurs at 732 m (~698 m true vertical depth), where the gradient decreases from >100°C/km to <50°C/km. This transition corresponds to an increase over a 5 m interval in both deep and shallow resistivity, a step-like increase in gamma, and an interval of mud loss, but is not otherwise recognized in the wireline data or fluid pressure data published by *Sutherland et al.* [2017]. The significance of this transition is discussed in the following section.

As illustrated in the inset in Figure 7, extrapolations of the temperature measurements made in DFDP-2B would intersect the boiling point for depth curve for pure water at depths of ~4 km, depending on the assumed gradient. The temperature also likely exceeds the illite–smectite transition within ~2 km of the surface.

3.4 Hydraulic observations

Figure 8 illustrates the progression of drilling and the mud level measurements recorded manually and automatically as indicators of borehole fluid loss or gain. The data used for slug test analyses were collected during pauses in drilling while mud was not being circulated. Also shown is the pressure measured at a fixed depth in the suction pit. Decreases in pressure correspond to the loss of mud, which we presume indicates flow out of the borehole and into the wallrock via permeable fractures. The mud pressure measurements in the suction pit revealed sporadic drops in pressure of several kilopascals. For a representative measured mud density of 1068 kg/m^3, a pressure drop of 1 kPa corresponds to a change in mud level of approximately 10 cm and, given the ~80 m^2 surface area of the suction pit, equates to a mud loss of approximately 8 m^3. On several occasions, pressure drops of 2–5 kPa or more occurred over intervals of only a few hours, indicating mud losses from the borehole into the formation of several tens of cubic meters or more.

Three representative slug test analyses from DFDP-2B are illustrated in Figure 9. The three tests illustrated were all conducted when the borehole had reached a depth of 396 m in a 133.5 m-long interval of open hole. The term *c* in the slug test analysis is the characteristic time over which the mud level varies. In the three cases illustrated, *c* appears to increase with time but this is not representative of the results overall. The 27 DFDP-2B slug tests yielding good fits to the simple decaying exponential model yield characteristic times of ~1–30 hours, with an average (the mean of the log of each value) of approximately 8.9 hours or 3.2×10^4 s. In other words, mud levels equilibrated rapidly implying the rock mass has a high hydraulic conductivity as discussed further below.

3.5 Fluid geochemistry

Mud gas monitoring revealed several zones of fluid influx, inferred from anomalies in Rn, CH_4, and to a lesser extent CO_2, H_2, and He (Figure 3). We interpret the discrete anomalies at 290 m (Rn), 400 m (CH_4), 430 m (CH_4, Rn), and 490 m (CH_4, Rn, H_2, He), and broader anomalies at 595–680 m (CH_4, CO_2, He, Rn?) and 760–820 m (CH_4, CO_2, Rn, H_2) to mark gas-permeable fractures. These depths correspond to zones of strong sonic attenuation, spikes in gamma and resistivity and, in the deepest case, to high BHTV reflectivity. There is no particularly consistent correspondence between gas anomalies and either mud loss or distinctive fracturing, although both He and Rn are elevated below ~590 m, where fracture densities are highest, and He in particular shows some correlation with fracture density.

4. Discussion

4.1 Petrophysical and structural characteristics of the hanging-wall

The wireline logging data illustrated in Figure 3 and Figure 4 exhibit only weak depth-related changes within the bedrock sequence in DFDP-2B: moreover, the systematic downward increases in gamma and deep resistivity in the DFDP-2B borehole (Figure 4) are much smaller than observed in DFDP-1B closer to the PSZ [*Townend et al.*, 2013]. This petrophysical homogeneity is consistent with the overall lithological homogeneity inferred from cuttings observations made with meter-scale resolution along the length of the borehole [*Toy et al.*, 2017]. Systematic changes in electrical properties were observed in DFDP-1B within ~30 m of the PSZ, and interpreted to arise from progressive alteration and precipitation of clays and other phyllosilicates [*Townend et al.*, 2013]. Since similar changes are not observed in The DFDP-2B logs, we infer this borehole did not get close enough to the PSZ for features associated with the alteration zone to be detected. This is again consistent with geological analyses of cuttings samples [*Toy et al.*, 2017].

Principal component analysis enables a dataset consisting of *p* measured parameters to be approximated by $r<p$ linear, orthogonal combinations of the original parameters, which are determined by eigenanalysis of the data correlation matrix [e.g. *Townend et al.*, 2013]. Here we analyze the correlation matrix formed of gamma, deep resistivity, deep/shallow resistivity and shear-wave measurements (i.e. p=4) acquired in the protomylonite interval at depths of 270–751 m (Figure 11).

The first principal component (PC1) is dominated by gamma and deep resistivity and accounts for ~43% of the total variance (**Error! Reference source not found.**, Supporting

Information Figure S2). We interpret PC1 to reflect changes in bulk lithology as the two parameters on which it most depends characterize the formation beyond the zone of drilling influence and on wavelengths of tens of centimeters that exceed the likely apertures of fractures based on BHTV analysis.

The second principal component (PC2) is dominated by the ratio of deep to shallow resistivity and accounts for 30% of the variance; and the third (PC3) is dominated by the shear-wave speed and accounts for a further 17% of the variance. PC2 exhibits an approximately linear depth-dependence (Figure 11), and PC2 and PC3 both reveal distinct transitions between ~500 and ~600 m (Supporting Information Figure S3). This latter change is particularly evident in PC3, and we hypothesize it relates to a change in the density of fractures manifest in the Vs and deep/shallow resistivity ratio data. The BHTV data show a general increase in fracture density below 600 m, although image quality was not sufficiently good between 550 and 600 m [due to presumed spalling of the borehole wall; *Massiot*, 2017] for any fractures to be picked there. The fourth principal component, PC4, accounts for the remaining 10% of the total variance, and like PC1 is dominated by parameters indicative of the formation (deep resistivity and gamma). More detailed analysis of the resistivity and sonic datasets has been undertaken, which will permit a more extensive analysis of the principal components and their variations in due course.

As noted in the previous section, a pronounced change in geothermal gradient occurs at a depth of approximately 732 m. The principal component analysis shows abrupt changes in all four principal components near this depth, and in PC1 and PC2 particularly. A notable mud loss occurred at this depth too. *Toy et al.* [2017] recognized compositional changes generally consistent with downwardly decreasing ratios of (quartz+feldspar) to mica but the cuttings sampling intervals and averaging preclude a detailed comparison with the logging data. Nevertheless, the coincidence of the change in gradient, mud loss, and a nearby change in inferred mineralogy suggests that 732 m corresponds to both a lithological and a hydraulic boundary. *Sutherland et al.* [2017] inferred it to be an aquitard, possibly a minor fault, separating two hydrogeological domains of different lithologies.

4.2 Evidence for an active hydrological system in the Alpine Fault's hanging-wall

Several lines of independent evidence suggest that the hanging-wall of the Alpine Fault is an active hydrogeologic system. Hot springs are the most obvious manifestation of the upper crustal circulation of meteoric fluids [*Cox et al.*, 2015; *Reyes et al.*, 2010], and the geochemistry of these fluids [*Menzies et al.*, 2014; *Menzies et al.*, 2016] and hydraulic measurements in the DFDP-1 boreholes [*Sutherland et al.*, 2012] reveal that the hanging- and footwalls of the Alpine Fault are hydrologically distinct.

DFDP-2B observations provide further evidence at <0.1–100 m scales that the rock mass has been subject to significant off-fault damage:

- Extensive fracturing inferred to represent both inherited (protolith) and fault-related processes;
- Fluid infiltration marked by gas anomalies;
- Abrupt mud losses of several cubic metres within hours; and
- Rapid (several-hour) mud level equilibration times.

Collectively, these conditions result in high hydraulic conductivity and an advection-dominated temperature regime and constitute what we refer to below as a "hydrogeologically active" system.

In comparison with measurements from other deep boreholes worldwide, the geothermal gradient measured in DFDP-2B during and after drilling is very high (125±55°C/km; Figure 7). *Sutherland et al.* [2017] interpreted the high geothermal gradient to reflect the combined effects of two advective processes: rock advection during uplift and exhumation and fluid advection produced by deep groundwater circulation and upwelling beneath the Whataroa valley. Given the strong lateral variations in groundwater flow patterns, the thermal regime is inferred to vary substantially in both the strike-parallel and strike-perpendicular directions. Variations in the cutoff depths of microseismicity southeast of the Alpine Fault have been hypothesized to reflect the thermal (and resistivity) structure [*Boese et al.*, 2012; *Bourguignon et al.*, 2015], but little quantitative analysis of the relationship between seismicity and temperature has been conducted here to date.

The BHTV dataset reveals pervasive fracturing with meter-scale spacing throughout the logged interval (Figure 3), with the exception of the poor-image-quality interval between ~550 and 590 m. The average orientations of the fractures and foliation features identified in the BHTV data set (Figure 6) are similar to one another, despite both sets of features exhibiting substantial scatter, and to the foliation orientations measured on nearby outcrops.

The mud loss data illustrated in Figure 8 imply that only a proportion of the intersected fractures are hydraulically conductive and that these features can transmit substantial fluid volumes within intervals of only a few hours. During drilling, mud losses could generally be remediated within ~30 minutes by the addition of bentonite, implying that the responsible fractures were rapidly sealed and that initial fracture permeabilities were even higher than inferred from subsequent slug tests. It is difficult to attribute mud losses recorded at the surface to specific fractures given the potential for simultaneous inward and outward flow at different depths. However, the inference of locally high fracture conductivity is consistent with the gas data indicating localized flow of pore fluids and the slug test analyses indicating mud level equilibration on timescales of hours (Figure 9).

Figure 10 illustrates the relationship between the characteristic time of a slug test response and hydraulic conductivity, based on the *Hvorslev* [1951] model. The characteristic times observed in DFDP-2B are of the order of hours (i.e. 10^4–10^5 s), and correspond to bulk hydraulic conductivities of the of order of 10^{-9} to 10^{-7} m/s. *Cox et al.* [2015] reported similar values of hydraulic conductivity for non-mylonitic schist in the hanging-wall of the Alpine Fault, in the Copland Valley, and even higher conductivities (10^{-6} m/s) in non-mylonitic schist sampled during exploratory hydroelectric drilling in the Amethyst Ravine. *Williams et al.* [2017b] noted that open fractures in the Amethyst cores were surrounded by alteration haloes characteristic of fluid flow. We hypothesize that the higher conductivities measured in the Amethyst Ravine to those in DFDP-2B or the Copland Valley represent topographically enhanced permeability: *Upton and Sutherland* [2014] showed that permeability controlled by a rock mass's proximity to frictional failure could account for variations in the temperatures measured in a tunnel. Their models showed permeability varying by a factor of >60 between areas of high topography, in which the rock mass was close to frictional failure in response to topographic stresses, and low topography (valley floors).

The non-mylonitic schist and protomylonite hydraulic conductivities summarized in Figure 10 all exceed, by several orders of magnitude, the conductivity of the brittle continental crust as a whole [~10^{-10} m/s; e.g. *Townend and Zoback*, 2000] or regionally metamorphosed rocks [~10^{-11} m/s; cf. *Manning and Ingebritsen*, 1999]. This emphasizes the role of damage associated with active faulting and geomorphic processes in increasing the hydraulic conductivity of the plate boundary zone at distances of at least several hundred meters from the principal slip zone [*Cox et al.*, 2015; *Roy et al.*, 2016; *Upton and Sutherland*, 2014].

4.3 Fault zone architecture and mechanical behavior

Prevailing models of fault zone architecture based on field observations of exhumed faults generally incorporate one or more low-permeability fault cores, within which localized or distributed strain has occurred, embedded within a high-permeability damage zone several tens to hundreds of meters in width, defined on the basis of fracture densities higher than those of the country rock [*Chester and Chester*, 2000; *Faulkner et al.*, 2011]. Such models typically treat the damage zone as a largely passive component of the fault zone in which deformation is induced by rupture propagation [*Dor et al.*, 2006] or stresses associated with geometric irregularities [*Faulkner et al.*, 2008],

In contrast to the damage zone widths inferred from geological observations, numerical simulations of earthquake rupture propagation increasingly highlight the mechanical significance of off-fault damage [*Ben-Zion and Shi*, 2005; *Ma*, 2008; *Templeton and Rice*, 2008] manifest as seismically and geodetically significant reductions in the fault zone's dynamic and static elastic moduli [*Cochran et al.*, 2009; *Fialko et al.*, 2002; *Xu et al.*, 2015]. Such damage typically exhibits a flower-shaped structure (viewed along strike) extending as much as several kilometers from the principal rupture surface [*Finzi et al.*, 2009], and affects both near-surface slip and rupture propagation [*Gabriel et al.*, 2013; *Kaneko and Fialko*, 2011] and near-field ground motion [*Andrews*, 2005; *Spudich and Olsen*, 2001]. The degree of off-fault damage is controlled by several factors including proximity to failure and the prevailing stress state [*Gabriel et al.*, 2013; *Sleep*, 2014; *Templeton and Rice*, 2008]. This suggests that the damage zone in areas of high topographic relief, characterized by lateral and vertical variations in both stress state [*Liu and Zoback*, 1992] and proximity to failure [*Koons et al.*, 2012; *Slim et al.*, 2015; *Upton and Sutherland*, 2014], is likely more complex than existing dynamic rupture models assume, particularly if the fault zone is rheologically asymmetric. Further complexity arises if active faults have time-varying hydraulic properties due to competition between processes of coseismic permeability enhancement and interseismic permeability reduction [e.g. *Finzi et al.*, 2011; *Sutherland et al.*, 2012].

Williams et al. [2017b] recently examined the geometric and mineralogical characteristics of fractures within the central Alpine Fault's damage zone using oriented cores and outcrop measurements. These analyses revealed little systematic change in fracture density with proximity to the PSZ; rather, the authors documented a 50–160 m-wide zone of variable fracture orientations on the hanging-wall side of the PSZ, beyond which an orientation similar to that of the schist protolith's foliation predominates. *Williams et al.* [2017b] interpreted the 50–160 m-wide zone of variable fracture orientations to correspond to the fault's damage zone (on the hanging-wall side), and noted that its width is consistent with those of the damage zones of large-displacement faults elsewhere [*Savage and Brodsky*, 2011]. The hanging-wall damage zone width reported by *Williams et al.* [2017b] is also similar to the width of the low-velocity zone inferred from fault zone guided wave measurements by *Eccles et al.* [2015], although the latter represents both hanging-wall and footwall damage.

The data presented here span ~700 m of the Alpine Fault's hanging-wall and are interpreted to extend to within ~200–400 m of the PSZ [*Toy et al.*, 2017]. This distance exceeds the maximum width of the damage zone reported by *Williams et al.* [2017b]. In addition, we do not observe a distinctive change in fracture characteristics (notwithstanding the BHTV dataset's resolution limits and the difficulty of distinguishing fractures from foliation) that would indicate that the outer margin of the damage zone has been crossed. However, based on the extensive fracturing, high thermal gradient, and high permeability, we infer that the entire DFDP-2B borehole lies within a hydrogeologically active zone of substantially greater width than either the damage zone as conventionally defined [*Faulkner et al.*, 2011; *Faulkner et al.*, 2010] or as measured for the Alpine Fault specifically [*Williams et al.*, 2017b].

The results of numerical modelling [*Sutherland et al.*, 2017] and the Amethyst hydraulic conductivity measurements exceeding 10^{-6} m/s made further than 2 km from the Alpine Fault's PSZ [*Cox et al.*, 2015] also suggest that a distinct, hydrogeologically active component of the fault exists that is at least ten times as wide as the damage zone documented by *Williams et al.* [2017b]. The state of stress in the Alpine Fault's hanging-wall likely varies substantially along- and across-strike due to catchment-scale variations in topographic relief and near-surface segmentation [*Barth et al.*, 2012; *Norris and Cooper*, 1995; *Upton et al.*, 2017]. Consequently, the proximity to failure and fracture permeability are both anticipated to vary laterally and vertically [*Upton and Sutherland*, 2014]. There are also large spatial gradients in the rates of interseismic shortening and shear strain in the hanging-wall within 10 km of the Alpine Fault trace [*Lamb and Smith*, 2013].

It is important to consider whether the width of the hydrogeologically active damage zone deduced from DFDP-2B observations reflects a peculiarity of the Whataroa Valley rather than the Alpine Fault itself. Site survey seismic data showed that there is no appreciable Quaternary (<16 kyr) offset of sediments next to the borehole, except possibly at the valley margin where topographically induced stress concentrations are greatest [*Upton et al.*, 2017]. There is a possibility that a south-dipping secondary reverse fault bounds the southern margin of the valley, which may be part of the reason for the greater-than-anticipated thickness of sediments encountered [*Jenkins*, 2016]. However, such a structure, if present, would be >100 m from the borehole and we would not expect to sample its damage zone. Thus, while there is the possibility of secondary faulting in the vicinity of the borehole, we do not consider this to account for the thickness of the damage zone. The Whataroa Valley also coincides with a junction between strike-slip and reverse segments of the Alpine Fault trace [*Barth et al.*, 2012; *Norris and Cooper*, 2001], which could enhance permeability via a pipe-like intersection. We do not consider this the explanation for the damage zone width observed, as high hydraulic conductivity is also inferred in the Amethyst and Copland Valleys (cf. Figure 10).

We cannot exclude the possibility that the Alpine Schist as a whole is highly permeable, and thus that the high hydraulic conductivities characteristic of the protomylonites encountered in DFPD-2B and the nonmylonitic schist encountered in the Amethyst tunnels are unrelated to the presence of the Alpine Fault. We consider this unlikely given the scale and thickness of the Alpine Schist as the bulk permeability of continental crust is of the order of 10^{-17} m^2 [e.g. *Townend and Zoback*, 2000], or a factor of at least 10–1000 less permeable than values estimated for the hanging-wall of the Alpine Fault. However, all of the locations at which the hydraulic conductivity of the Alpine Schist and the related Otago schist has been estimated, including those described above and active landslides surrounding the Clyde Dam in central Otago [*O'Brien et al.*, 2016], yield higher conductivities than typical of regionally metamorphosed rocks [e.g. *Manning and Ingebritsen*, 1999]. No measurements of the schist's permeability have yet been made away from a major fault or landside: such measurements would enable the bulk permeability of the protolith to be estimated, and thus the significance of fault-related and non-fault-related (static) effects to be distinguished.

Our preferred interpretation of the apparent width of the hydrogeologically active damage zone is that it is controlled by the interaction of the Alpine Fault with topography. We propose a model of the hydrogeologically active damage zone that may also apply to faults in other areas of pronounced topographic relief, oblique slip and recurring seismicity (Figure 12). We distinguish between an inner damage zone of width 10^{-1}–10^{2} m, in which fracturing is induced by dynamic stresses associated with the rupture process, and an outer damage zone of width 10^{3}–10^{4} m, within which damage reflects a juxtaposition of fracturing associated with exhumation, recurring phases of interseismic strain accumulation and release, and coseismic-shaking-induced slip on critically-stressed fractures. In the context of this model, the inner damage zone corresponds to the conventionally defined damage zone inferred from field observations of fracture density, whereas the outer damage zone corresponds to the flower-shaped zone of low elastic moduli inferred from seismological and geodetic observations.

The model implies fault zone asymmetry that is likely governed by topographic relief and the kinematics of slip, with faults accommodating oblique transpression, such as the central Alpine Fault, having broader hanging-wall damage zones than areas of pure strike-slip, perhaps including the southern section of the Alpine Fault. A testable corollary is that the inner and outer damage zones should exhibit different types of fracturing: dilatant, low shear-displacement factures in the inner zone associated with rupture propagation, and preferentially oriented shear fractures in the outer zone that represent failure of the most critically-stressed structures in response to shaking.

The implications of an active hydrologic system in the hanging-wall of the Alpine Fault late in the fault's typical interseismic phase are significant. At present, the fluid pressure regime in the hanging-wall exhibits modest spatial variations about hydrostatic levels (being sub-hydrostatic beneath the mountains to permit downward flow and ~10% over-pressured in DFDP-2B), implying high effective stresses [*Sutherland et al.*, 2017]. Different portions of the damage zone are also likely to undergo temporal changes in hydraulic parameters and flow, due to competing processes of fracture sealing and opening or re-opening at different points in the seismic cycle [*Hacker*, 1997; *Sibson*, 1989; 1994]. The precipitation of calcite, quartz, and other phases, and the resulting decrease in permeability, likely occurs throughout the fault zone [*Boulton et al.*, 2017a; *Boulton et al.*, 2017b; *Williams et al.*, 2017a]. However, our observations show that, even late in the interseismic cycle, the outer damage zone retains substantial permeability and an approximately hydrostatic fluid pressure regime in the hanging-wall.

The low permeability of the alteration zone and fault core documented in DFDP-1 [*Allen et al.*, 2017; *Boulton et al.*, 2017a; *Carpenter et al.*, 2014; *Sutherland et al.*, 2012] and the different piezometric heights of the high-relief hanging-wall and low-relief footwall do imply substantial variations in fluid pressure and hence in effective stress across the PSZ. The extremely low permeability and meter-scale width of the fault core are likely to play a significant role in governing earthquake rupture on the central Alpine Fault [*Sutherland et al.*, 2012]. In particular, the very low permeability of $<10^{-20}$ m^2 (equivalent to a hydraulic conductivity of $<10^{-13}$ m/s) estimated for the 2 m-thick fault core from post-drilling fluid pressure equilibration measurements in the DFDP-1B borehole suggests that the fault may undergo thermal pressurization or vaporisation in response to small amounts (possibly submillimeter) of slip at low slip rates (<1 mm/s) well before the onset of seismic radiation [*Boulton et al.*, 2017c; *Chen et al.*, 2017; *Schmitt et al.*, 2011; *Segall and Rice*, 2006].

5. Conclusions

DFDP-2B measurements and observations made previously at outcrop and catchment scales reveal the hanging-wall of the central Alpine Fault to contain an active hydrothermal circulation system: temperatures and permeability are high and fluid pressures exceed hydrostatic values due to upflow beneath the Whataroa Valley. Independent lines of evidence — borehole temperature measurements, gas geochemistry, fracture orientation and density data sets, and known hot springs — indicate that fault-related damage and fluid circulation extend at least several hundred meters from the principal slip zone. This suggests that the hydrogeologically active component of the Alpine Fault zone, in the hanging-wall at least, is both wider and more dynamic (in the sense of controlling fluid pressures and temperatures) than implied by prevailing models of faults' damage zones.

We propose that the hydrogeologically active hanging-wall damage zone of the Alpine Fault (and likely those of other large active faults in areas of high topographic relief and rapid slip) is composed of an inner damage zone in which damage is dominated by rupture processes, and an outer damage zone in which damage reflects processes occurring on long-term (exhumational), interseismic, and coseismic time-scales. This model provides a means of reconciling the generally narrow (10^1–10^2 m-wide) damage zones identified from analysis of fracturing adjacent to exhumed faults with the broader (10^3–10^4 m-wide) damage zones inferred from seismological and geodetic data.

Acknowledgments

We are grateful to the Friend family for land access and to the Whataroa community for long-standing support. This manuscript benefited from thought-provoking critiques by Toru Takeshita, Bob Holdsworth, and an anonymous reviewer. Core funding for DFDP-2 was provided by the International Continental Scientific Drilling Program (ICDP), the Marsden Fund of the Royal Society of New Zealand, GNS Science, Victoria University of Wellington, the University of Otago, the Ministry of Business, Innovation and Employment, and NERC grants NE/J022128/1 and NE/J024449/1.

Author contributions

The DFDP-2 drilling experiment was led by Sutherland, Townend, and Toy. All authors except Hartog, Pezard, Remaud, and Teagle were present on site and all authors contributed to data collection and interpretation during drilling. Post-drilling analysis of the wireline and hydraulic data sets was coordinated by Coussens, Doan and Remaud, Jeppson, and Massiot, and manuscripts describing those results are in preparation.

Data access

The data used in this study are available on request from the corresponding author. Further details regarding data acquisition are available in the DFDP-2 completion report [*Sutherland et al.*, 2015].

Table 1. Principal component analysis of the wireline logging data from DFDP-2B in the depth interval 270–751 m.

Parameter	PC1	PC2	PC3	PC4
Gamma (API)	0.63	–0.10	–0.50	–0.58
DLL (Deep, Ω·m)	0.64	0.27	–0.07	0.71
DLL (Deep/Shallow)	0.13	0.79	0.46	–0.38
V_S (m/s)	0.41	–0.53	0.73	–0.09
Eigenvalue	1.70	1.22	0.67	0.40
Cumulative percentage explained	42.5%	73.1%	90.0%	100.0%

Figure 1. Location map showing the position of the DFDP-1 and DFDP-2 drill sites (white circles), mapped faults (red and dashed black lines), thermal springs (red dots), and cover and basement lithostratigraphy (background colors). The inset shows the location of the main map and the distribution of the Alpine Schist (purple) and thermal springs (red dots). The thermal springs shown are in some cases ephemeral [*Reyes et al.*, 2010].

Figure 2. DFDP-2B lithostratigraphy and drilling and completion schematic. The vertical scale shows measured depth. ID — inner diameter. OD — outer diameter.

Figure 3. Composite wireline figure summarizing petrophysical, geochemical, and hydraulic measurements made in the DFDP-2B borehole. The vertical scale on the left-hand side shows measured depth; the right-hand scale shows true vertical depth (i.e. after correction for borehole deviation). From left to right: measured depth; rate of progression (ROP) and mud loss during drilling; borehole diameter, bit size, and bit changes; natural gamma; H_2, CO_2, and CH_4 concentrations in mud gas; He and Rn concentrations in mud gas; deep and shallow resistivity, and deep/shallow (D/S) ratio; temperature measured with DTS; temperature gradient; full-waveform sonic traces; Vp, Vs, and Vp/Vs ratio; normalized BHTV amplitudes; numbers of fractures and foliations in 10 m intervals; true vertical depth; lithology.

Figure 4. Gamma and resistivity data showing (left) the repeatability of median-filtered gamma logs and (center, right) similarities in the composite gamma and deep dual-laterolog resistivity curves acquired in successive logging runs 49 (gamma) and 50 (DLL). The black squares in the middle and right-hand panels mark the 732 m depth of the change in geothermal gradient (Figure 3). The gamma data were acquired in two downward passes (passes 1 and 2) at nominal logging speeds of 4–18 m/min and one upward pass (pass 3) at 4 m/min. The DLL data were acquired at 20 m/min while logging upwards.

Figure 5. Wireline data detail and interpretation of structural features imaged with BHTV. From left to right: measured depth, borehole caliper and bit diameter; repeated deep and shallow resistivity logs; ratio of deep to shallow resistivity (D/S); full-waveform seismic traces; normalized BHTV travel-time; normalized BHTV amplitude; 3D representation of the borehole looking towards an azimuth of 028°; tadpole plot showing the dips and dip directions of foliation and fracture features; foliation and fracture counts in 10 m depth intervals; DTS temperature and repeated temperature gradient measurements; true vertical depth. The depth interval illustrated in this figure lies entirely within the protomylonite zone (see Figure 3).

Figure 6. Lower hemisphere, equal-area stereonet showing orientations of foliation (mauve squares) and fractures (pink circles) identified in DFDP-2B BHTV logs and other structural datasets. The large squares and corresponding great circles indicate the mean orientations of the foliation (mauve) and fractures (pink). TS — mean foliation of 053/63 measured in Tatare Stream outcrops [*Gillam et al.*, 2014]; WF — mean foliation of 055/50 measured in Whataroa Valley outcrops [*Little et al.*, 2002a]; AF — representative Alpine orientation of 055/50 [*Norris and Cooper*, 2007]. All orientations are expressed as strike/dip, using the convention that all dips are to the right when looking along strike. The borehole trajectory is sub-vertical to ~300 m, then deviates steadily towards the NNW (diamonds, plotted at 100 m intervals from 300 m).

Figure 7. Temperature logs and projections. Left: the colored lines represent successive temperature logs acquired during drilling using wireline tools and the thick black line shows

the equilibrated temperature profile measured several times between January and September 2015 using the optical fiber installed in the borehole and a distributed temperature sensing (DTS) interrogator [*Sutherland et al.*, 2017]. The dashed lines indicate gradients of 50, 100, and 150°C/km for comparison; the gradient measured in DFDP-1B was 62°C/km [*Sutherland et al.*, 2012]. Right: expanded view of the left-hand figure showing the DTS curve (black line), the boiling point for depth curve calculated for pure water (dashed red line), and the indicative temperature range over which illite alters to smectite (pink swath) [*Pytte and Reynolds*, 1989].

Figure 8. Summary of (top to bottom) progression of drilling, manual mud level measurements made within the borehole, and suction pit pressure measurements used to identify times of mud loss.

Figure 9. Three representative slug test measurements acquired after the DFDP-2B borehole had reached a depth of 396.8 m, and corresponding best-fitting exponential models. In each case, the length of open borehole during the test was 133.5 m. The vertical axis of each plot shows the height of the mud relative to a reference level at the top of the borehole. The slug tests illustrated are ST05 (a=–7.5 m, b=6.6 m, c=1.7 hr, R^2=0.96), ST07 (a=–4.1 m, b=3.7 m, c=6.4 hr, R^2=0.99), and ST11 (a=–0.43 m, b=–1.9 m, c=21 hr, R^2=0.99). The last of these represents flow into the borehole.

Figure 10. Summary of hydraulic conductivity estimates from DFDP-2B and other locations near the Alpine Fault. The right-hand vertical axis shows corresponding permeability values calculated assuming the viscosity and density of pure water. The diagonal lines show hydraulic conductivity vs. characteristic time curves (parameter c in the analyses shown in Figure 9) for an idealized slug test model [*Hvorslev*, 1951] for different test interval lengths (L) representative of the measurements made in DFDP-2B and presumed effective borehole radii (R_e). Other parameters: r_e = 0.13 m and r_w = 0.11 m (corresponding to the radii of the 10” cased interval in which the mud levels were measured and the 8.5” drilled interval, respectively). Also shown are the average (mean of $\log_{10}$ values) and ranges (±standard deviation of $\log_{10}$ values) of the characteristic times observed in DFDP-2B slug tests; previously published hydraulic conductivity values of 10^{-8} to 10^{-5} m/s for Alpine Schist in the mountains surrounding the Copland Valley and of (0.6–3.5)×10^{-5} m/s for boreholes drilled in the Amethyst Ravine hydroelectricity project [*Cox et al.*, 2015]; and a representative value for the average hydraulic conductivity of the brittle crust (10^{-10} m/s, equivalent to permeability of 10^{-17} m^2) [*Townend and Zoback*, 2000].

Figure 11. Results of principal component analysis applied to the correlation matrix of the matrix containing gamma, deep resistivity, deep/shallow resistivity, and shear-wave measurements in the depth interval 270–751 m. The upper row of graphs shows the input data and the lower row shows the corresponding four principal components, both as functions of depth. The input data have been filtered using a fifth-order median filter applied to a running 2.5 m-long window to remove high-frequency signals. Also shown are the depths of mud level anomalies, colored red (major), green (moderate), and blue (minor).

Figure 12. Schematic fault zone diagram [modified after *Sutherland et al.*, 2012] illustrating the extent of the hydrogeologically active damage zone and its subdivision into inner and outer damage zones. Also illustrated is the approximate vertical extent of topographic stress perturbations beneath fault-perpendicular ridges in the hanging-wall. The flower-shaped geometry of the outer damage zone is controlled by interaction between stress changes

occurring on coseismic and interseismic timescales and critically-stressed fractures subject to frictional failure under the combined effects of topographic and tectonic loading.

References

Allen, M. J., D. Tatham, D. R. Faulkner, E. Mariani, and C. Boulton (2017), Permeability and seismic velocity and their anisotropy across the Alpine Fault, New Zealand: An insight from laboratory measurements on core from the Deep Fault Drilling Project phase 1 (DFDP-1), *Journal of Geophysical Research: Solid Earth*.

Allis, R. G., and Y. Shi (1995), New insights to temperature and pressure beneath the central Southern Alps, New Zealand, *New Zealand Journal of Geology and Geophysics*, *38*(4), 585–592.

Andrews, D. J. (2005), Rupture dynamics with energy loss outside the slip zone, *Journal of Geophysical Research: Solid Earth*, *110*(B1), n/a-n/a.

Barber, T., and W. A. Griffith (2017), Experimental constraints on dynamic fragmentation as a dissipative process during seismic slip, *Philosophical Transactions of the Royal Society A: Mathematical, Physical and Engineering Sciences*, *375*(2103).

Barth, N. C., V. G. Toy, R. M. Langridge, and R. J. Norris (2012), Scale dependence of oblique plate-boundary partitioning: New insights from LiDAR, central Alpine fault, New Zealand, *Lithosphere*, *4*(5), 435-448.

Barth, N. C., C. Boulton, B. M. Carpenter, G. E. Batt, and V. G. Toy (2013), Slip localization on the southern Alpine Fault, New Zealand, *Tectonics*, *32*(3), 620-640.

Ben-Zion, Y., and Z. Q. Shi (2005), Dynamic rupture on a material interface with spontaneous generation of plastic strain in the bulk, *Earth and Planetary Science Letters*, *236*(1-2), 486-496.

Berryman, K. R., U. A. Cochran, K. J. Clark, G. P. Biasi, R. M. Langridge, and P. Villamor (2012), Major earthquakes occur regularly on an isolated plate boundary fault, *Science*, 1690-1693, doi: 10.1126/science.1218959.

Biasi, G. P., R. M. Langridge, K. R. Berryman, K. J. Clark, and U. A. Cochran (2015), Maximum-Likelihood Recurrence Parameters and Conditional Probability of a Ground-Rupturing Earthquake on the Southern Alpine Fault, South Island, New Zealand, *Bulletin of the Seismological Society of America*.

Bleibinhaus, F., J. A. Hole, T. Ryberg, and G. S. Fuis (2007), Structure of the California Coast Ranges and San Andreas Fault at SAFOD from seismic waveform inversion and reflection imaging, *Journal of Geophysical Research: Solid Earth*, *112*(6).

Boese, C. M., J. Townend, E. Smith, and T. Stern (2012), Microseismicity and stress in the vicinity of the Alpine Fault, central Southern Alps, New Zealand, *Journal of Geophysical Research: Solid Earth*, *117*(2).

Boese, C. M., T. A. Stern, J. Townend, S. Bourguignon, A. Sheehan, and E. G. C. Smith (2013), Sub-crustal earthquakes within the Australia-Pacific plate boundary zone beneath the Southern Alps, New Zealand, *Earth and Planetary Science Letters*, *376*, 212-219.

Boulton, C., L. Janku-Capova, J. N. Williams, and J. P. Coussens (2017a), A window into thousands of earthquakes: results from the Deep Fault Drilling Project (DFDP), *New Zealand Science Review*, *74*, 27-35.

Boulton, C., C. D. Menzies, V. G. Toy, J. Townend, and R. Sutherland (2017b), Geochemical and microstructural evidence for interseismic changes in fault zone permeability and strength, Alpine Fault, New Zealand, *Geochemistry, Geophysics, Geosystems*, *18*(1), 238-265.

Boulton, C., D. E. Moore, D. A. Lockner, V. G. Toy, J. Townend, and R. Sutherland (2014), Frictional properties of exhumed fault gouges in DFDP-1 cores, Alpine Fault, New Zealand, *Geophysical Research Letters*, *41*(2), 356-362.

Boulton, C., L. Yao, D. R. Faulkner, J. Townend, V. G. Toy, R. Sutherland, S. Ma, and T. Shimamoto (2017c), High-velocity frictional properties of Alpine Fault rocks: Mechanical data, microstructural analysis, and implications for rupture propagation, *Journal of Structural Geology*, *97*, 71-92.

Bourguignon, S., S. Bannister, C. M. Henderson, J. Townend, and H. Zhang (2015), Structural heterogeneity of the midcrust adjacent to the central Alpine Fault, New Zealand: Inferences from seismic tomography and seismicity between Harihari and Ross, *Geochemistry, Geophysics, Geosystems*, *16*(4), 1017-1043.

Bouwer, H., and R. C. Rice (1976), A slug test for determining hydraulic conductivity of unconfined aquifers with completely or partially penetrating wells, *Water Resources Research*, *12*(3), 423-428.

Caine, J. S., J. P. Evans, and C. B. Forster (1996), Fault zone architecture and permeability structure, *Geology*, *24*(11), 1025-1028.

Carpenter, B. M., H. Kitajima, R. Sutherland, J. Townend, V. G. Toy, and D. M. Saffer (2014), Hydraulic and acoustic properties of the active Alpine Fault, New Zealand: Laboratory measurements on DFDP-1 drill core, *Earth and Planetary Science Letters*, *390*, 45-51.

Chamberlain, C. J., C. M. Boese, and J. Townend (2017), Cross-correlation-based detection and characterisation of microseismicity adjacent to the locked, late-interseismic Alpine Fault, South Westland, New Zealand, *Earth and Planetary Science Letters*, *457*, 63-72.

Chamberlain, C. J., D. R. Shelly, J. Townend, and T. A. Stern (2014), Low-frequency earthquakes reveal punctuated slow slip on the deep extent of the Alpine Fault, New Zealand, *Geochemistry, Geophysics, Geosystems*, *15*(7), 2984-2999.

Chen, J., A. Niemeijer, L. Yao, and S. Ma (2017), Water vaporization promotes coseismic fluid pressurization and buffers temperature rise, *Geophysical Research Letters*, *44*(5), 2177-2185.

Chester, F. M., and J. S. Chester (2000), Stress and deformation along wavy frictional faults, *Journal of Geophysical Research: Solid Earth*, *105*(B10), 23421-23430.

Cochran, E. S., Y.-G. Li, P. M. Shearer, S. Barbot, Y. Fialko, and J. E. Vidale (2009), Seismic and geodetic evidence for extensive, long-lived fault damage zones, *Geology*, *37*(4), 315-318.

Cochran, U. A., K. J. Clark, J. D. Howarth, G. P. Biasi, R. M. Langridge, P. Villamor, K. R. Berryman, and M. J. Vandergoes (2017), A plate boundary earthquake record from a wetland adjacent to the Alpine fault in New Zealand refines hazard estimates, *Earth and Planetary Science Letters*, *464*, 175-188.

Cox, S. C., and D. J. A. Barrell (2007), Geology of the Aoraki area, in *Institute of Geological and Nuclear Sciences 1:250000 Geological Map*, edited, p. 71, GNS Science, Lower Hutt.

Cox, S. C., C. D. Menzies, R. Sutherland, P. H. Denys, C. Chamberlain, and D. A. H. Teagle (2015), Changes in hot spring temperature and hydrogeology of the Alpine Fault hanging wall, New Zealand, induced by distal South Island earthquakes, *Geofluids*, *15*(1-2), 216-239.

Dor, O., Y. Ben-Zion, T. K. Rockwell, and J. Brune (2006), Pulverized rocks in the Mojave section of the San Andreas Fault Zone, *Earth and Planetary Science Letters*, *245*(3-4), 642-654, doi: 10.1016/j.epsl.2006.03.034.

Eccles, J. D., A. K. Gulley, P. E. Malin, C. M. Boese, J. Townend, and R. Sutherland (2015), Fault Zone Guided Wave generation on the locked, late interseismic Alpine Fault, New Zealand, *Geophysical Research Letters*, *42*(14), 5736-5743.

Ellis, D. V., J. M. Singer, and SpringerLink (Online service) (2007), Well Logging for Earth Scientists, edited, Springer Science+Business Media B.V., Dordrecht.

Erzinger, J., T. Wiersberg, and M. Zimmer (2006), Real-time mud gas logging and sampling during drilling, *Geofluids*, *6*(3), 225-233.

Faulkner, D. R., T. M. Mitchell, E. H. Rutter, and J. Cembrano (2008), On the structure and mechanical properties of large strike-slip faults, *Geological Society, London, Special Publications*, *299*(1), 139-150.

Faulkner, D. R., T. M. Mitchell, E. Jensen, and J. Cembrano (2011), Scaling of fault damage zones with displacement and the implications for fault growth processes, *Journal of Geophysical Research: Solid Earth*, *116*(B5), n/a-n/a.

Faulkner, D. R., C. A. L. Jackson, R. J. Lunn, R. W. Schlische, Z. K. Shipton, C. A. J. Wibberley, and M. O. Withjack (2010), A review of recent developments concerning the structure, mechanics and fluid flow properties of fault zones, *Journal of Structural Geology*, *32*(11), 1557-1575.

Feenstra, J., C. Thurber, J. Townend, S. Roecker, S. Bannister, C. Boese, N. Lord, S. Bourguignon, and D. Eberhart-Phillips (2016), Microseismicity and P–wave tomography of the central Alpine Fault, New Zealand, *New Zealand Journal of Geology and Geophysics*, 1-13.

Fialko, Y., D. Sandwell, D. Agnew, M. Simons, P. Shearer, and B. Minster (2002), Deformation on nearby faults induced by the 1999 Hector Mine earthquake, *Science*, *297*(5588), 1858-1862.

Finzi, Y., E. H. Hearn, Y. Ben-Zion, and V. Lyakhovsky (2009), Structural Properties and Deformation Patterns of Evolving Strike-slip Faults: Numerical Simulations Incorporating Damage Rheology, *Pure and Applied Geophysics*, *166*(10), 1537-1573.

Finzi, Y., E. H. Hearn, V. Lyakhovsky, and L. Gross (2011), Fault-zone healing effectiveness and the structural evolution of strike-slip fault systems, *Geophysical Journal International*, *186*(3), 963-970.

Gabriel, A. A., J. P. Ampuero, L. A. Dalguer, and P. M. Mai (2013), Source properties of dynamic rupture pulses with off-fault plasticity, *Journal of Geophysical Research: Solid Earth*, *118*(8), 4117-4126.

Gillam, B. G., T. A. Little, E. Smith, and V. G. Toy (2014), Extensional shear band development on the outer margin of the Alpine mylonite zone, Tatare Stream, Southern Alps, New Zealand, *Journal of Structural Geology*, *64*, 115-134.

Guo, B., C. H. Thurber, S. W. Roecker, J. Townend, C. Rawles, C. J. Chamberlain, C. M. Boese, S. Bannister, J. Feenstra, and J. D. Eccles (2017), 3-D P- and S-wave velocity structure along the central Alpine Fault, South Island, New Zealand, *Geophysical Journal International*, *209*(2), 935-947.

Hacker, B. R. (1997), Diagenesis and fault valve seismicity of crustal faults, *Journal of Geophysical Research B: Solid Earth*, *102*(11), 24459-24467.

Hobbs, B., and A. Ord (2015), *Structural Geology*, 665 pp., Elsevier, Oxford.

Howarth, J. D., S. J. Fitzsimons, R. J. Norris, and G. E. Jacobsen (2012), Lake sediments record cycles of sediment flux driven by large earthquakes on the Alpine fault, New Zealand, *Geology*, *40*(12), 1091-1094.

Howarth, J. D., S. J. Fitzsimons, R. J. Norris, and G. E. Jacobsen (2014), Lake sediments record high intensity shaking that provides insight into the location and rupture length of large earthquakes on the Alpine Fault, New Zealand, *Earth and Planetary Science Letters*, *403*, 340-351.

Howarth, J. D., S. J. Fitzsimons, R. J. Norris, R. Langridge, and M. J. Vandergoes (2016), A 2000 yr rupture history for the Alpine fault derived from Lake Ellery, South Island, New Zealand, *GSA Bulletin*, *128*(3-4), 627-643.

Hvorslev, M. J. (1951), Time lag and soil permeability in groundwater observations*Rep.*, 56 pp, U.S. Army Corps of Engineers, Waterways Experimental Station, Vicksberg, MS.

Jenkins, S. (2016), A gravity analysis of the Alpine Fault and the DFDP-2 drill site, Whataroa valley, South Westland, South Island, New Zealand, MSc thesis, 241 pp, Victoria University of Wellington, https://researcharchive.vuw.ac.nz/handle/10063/6459.

Kaneko, Y., and Y. Fialko (2011), Shallow slip deficit due to large strike-slip earthquakes in dynamic rupture simulations with elasto-plastic off-fault response, *Geophysical Journal International*, *186*(3), 1389-1403.

Koons, P. O. (1987), Some thermal and mechanical consequences of rapid uplift; an example from the Southern Alps, New Zealand, *Earth and Planetary Science Letters*, *86*(2), 307–319.

Koons, P. O., P. Upton, and A. D. Barker (2012), The influence of mechanical properties on the link between tectonic and topographic evolution, *Geomorphology*, *137*(1), 168-180.

Koons, P. O., D. Craw, S. C. Cox, P. Upton, A. S. Templeton, and C. P. Chamberlain (1998), Fluid flow during active oblique convergence: A Southern Alps model from mechanical and eeochemical observations, *Geology*, *26*(2), 159–162.

Lamb, S., and E. Smith (2013), The nature of the plate interface and driving force of interseismic deformation in the New Zealand plate-boundary zone, revealed by the continuous GPS velocity field, *Journal of Geophysical Research: Solid Earth*, *118*(6), 3160-3189.

Little, T. A., R. J. Holcombe, and B. R. Ilg (2002a), Kinematics of oblique collision and ramping inferred from microstructures and strain in middle crustal rocks, Central Southern Alps, New Zealand, *Journal of Structural Geology*, *24*(1), 219-239.

Little, T. A., R. J. Holcombe, and B. R. Ilg (2002b), Ductile fabrics in the zone of active oblique convergence near the Alpine Fault, New Zealand: Identifying the neotectonic overprint, *Journal of Structural Geology*, *24*(1), 193-217.

Little, T. A., S. Cox, J. K. Vry, and G. Batt (2005), Variations in exhumation level and uplift rate along the oblique-slip Alpine fault, central Southern Alps, New Zealand, *Bulletin of the Geological Society of America*, *117*(5-6), 707-723.

Liu, L., and M. D. Zoback (1992), The effect of topography on the state of stress in the crust: application to the site of the Cajon Pass Scientific Drilling Project, *Journal of Geophysical Research*, *97*(B4), 5095-5108.

Ma, S. (2008), A physical model for widespread near-surface and fault zone damage induced by earthquakes, *Geochemistry, Geophysics, Geosystems*, *9*(11).

Manning, C. E., and S. E. Ingebritsen (1999), Permeability of the continental crust: Implications of geothermal data and metamorphic systems, *Reviews of Geophysics*, *37*(1), 127-150.

Massiot, C. (2017), Fracture system characterisation and implications for fluid flow in volcanic and metamorphic rocks, PhD thesis, 191 pp, Victoria University of Wellington, http://hdl.handle.net/10063/6194.

Menzies, C. D., D. A. H. Teagle, D. Craw, S. C. Cox, A. J. Boyce, C. D. Barrie, and S. Roberts (2014), Incursion of meteoric waters into the ductile regime in an active orogen, *Earth and Planetary Science Letters*, *399*, 1-13.

Menzies, C. D., D. A. H. Teagle, S. Niedermann, S. C. Cox, D. Craw, M. Zimmer, M. J. Cooper, and J. Erzinger (2016), The fluid budget of a continental plate boundary fault: Quantification from the Alpine Fault, New Zealand, *Earth and Planetary Science Letters*.

Norris, R. J., and A. F. Cooper (1995), Origin of small-scale segmentation and transpressional thrusting along the Alpine Fault, New Zealand, *Geological Society of America Bulletin*, *107*(2), 231–240.

Norris, R. J., and A. F. Cooper (2001), Late Quaternary slip rates and slip partitioning on the Alpine Fault, New Zealand, *Journal of Structural Geology*, *23*(2-3), 507–520.

Norris, R. J., and A. F. Cooper (2007), The Alpine Fault, New Zealand: surface geology and field relationships, in *A Continental Plate Boundary: Tectonics at South Island, New Zealand*, edited by D. Okaya, T. A. Stern and F. Davey, pp. 157–175, American Geophysical Union.

O'Brien, G. A., S. C. Cox, and J. Townend (2016), Spatially and temporally systematic hydrologic changes within large geoengineered landslides, Cromwell Gorge, New Zealand, induced by multiple regional earthquakes, *Journal of Geophysical Research: Solid Earth, 121*(12), 8750-8773.

Papadopulos, S. S., J. D. Bredehoeft, and H. H. Cooper (1973), On the analysis of 'slug test' data, *Water Resources Research, 9*(4), 1087-1089.

Pezard, P. A., and R. N. Anderson (1990), In Situ Measurements Of Electrical Resistivity, Formation Anisotropy, And Tectonic Context, edited, Society of Petrophysicists and Well-Log Analysts.

Pytte, A. M., and R. C. Reynolds (1989), The Thermal Transformation of Smectite to Illite, in *Thermal History of Sedimentary Basins: Methods and Case Histories*, edited by N. D. Naeser and T. H. McCulloh, pp. 133-140, Springer New York, New York, NY.

Reid, J. J. (1964), Mylonites, cataclasites, and associated rocks along the Alpine Fault, South Island, New Zealand, *New Zealand Journal of Geology and Geophysics*, *7,* 645–684.

Remaud, L. (2015), Study of the damage zone around the Alpine Fault, New Zealand, from borehole data of the Deep Fault Drilling Project (stage 2), MSc thesis, 61 pp, Université Joseph Fourier, Grenoble.

Reyes, A. G., B. W. Christenson, and K. Faure (2010), Sources of solutes and heat in low-enthalpy mineral waters and their relation to tectonic setting, New Zealand, *Journal of Volcanology and Geothermal Research*, *192*(3-4), 117-141.

Rice, J. R., and M. Cocco (2007), Seismic fault rheology and earthquake dynamics, in *Tectonic faults: agents of change on a dynamic earth*, edited by M. R. Handy, G. Hirth and N. Hovius, pp. 99–137, The MIT Press, Cambridge, MA.

Roy, S. G., G. E. Tucker, P. O. Koons, S. M. Smith, and P. Upton (2016), A fault runs through it: Modeling the influence of rock strength and grain-size distribution in a fault-damaged landscape, *Journal of Geophysical Research F: Earth Surface*, *121*(10), 1911-1930.

Savage, H. M., and E. E. Brodsky (2011), Collateral damage: Evolution with displacement of fracture distribution and secondary fault strands in fault damage zones, *Journal of Geophysical Research: Solid Earth*, *116*(B3).

Schleicher, A. M., R. Sutherland, J. Townend, V. G. Toy, and B. A. van der Pluijm (2015), Clay mineral formation and fabric development in the DFDP-1B borehole, central Alpine Fault, New Zealand, *New Zealand Journal of Geology and Geophysics*, 1-9.

Schmitt, S. V., P. Segall, and T. Matsuzawa (2011), Shear heating-induced thermal pressurization during earthquake nucleation, *Journal of Geophysical Research B: Solid Earth*, *116*(6).

Segall, P., and J. R. Rice (2006), Does shear heating of pore fluid contribute to earthquake nucleation?, *Journal of Geophysical Research B: Solid Earth*, *111*(9).

Shi, Y., R. G. Allis, and F. Davey (1996), Thermal modelling of the Southern Alps, New Zealand, *Pure and Applied Geophysics, 146*, 469–501.

Sibson, R. H. (1989), Earthquake faulting as a structural process, *Journal of Structural Geology*, *11*(1-2), 1-14.

Sibson, R. H. (1994), Crustal stress, faulting and fluid flow, in *Geological Society Special Publication*, edited, pp. 69-84.

Sibson, R. H., S. H. White, and B. K. Atkinson (1981), Structure and distribution of fault rocks in the Alpine fault zone, New Zealand, in *Thrust and nappe tectonics*, edited by K. R. McClay and N. J. Price, pp. 197–210, Geological Society of London, London.

Sleep, N. H. (2014), Ambient tectonic stress as fragile geological feature, *Geochemistry, Geophysics, Geosystems*, *15*(9), 3628-3644.

Slim, M., J. T. Perron, S. J. Martel, and K. Singha (2015), Topographic stress and rock fracture: a two-dimensional numerical model for arbitrary topography and preliminary comparison with borehole observations, *Earth Surface Processes and Landforms*, *40*(4), 512-529.

Spudich, P., and K. B. Olsen (2001), Fault zone amplified waves as a possible seismic hazard along the Calaveras fault in central California, *Geophysical Research Letters*, *28*(13), 2533-2536.

Sutherland, R., J. Townend, V. G. Toy, and e. al. (2017), Extreme hydrothermal conditions at an active plate-bounding fault, doi: 10.1038/nature22355.

Sutherland, R., et al. (2007), Do great earthquakes occur on the Alpine fault in central South Island, New Zealand?, in *A Continental Plate Boundary: Tectonics at South Island, New Zealand*, edited by D. Okaya, T. A. Stern and F. Davey, pp. 235–251, American Geophysical Union.

Sutherland, R., et al. (2012), Drilling reveals fluid control on architecture and rupture of the Alpine fault, New Zealand, *Geology*, *40*(12), 1143-1146.

Sutherland, R., et al. (2011), Operations and well completion report for boreholes DFDP-1A and DFDP-1B, Deep Fault Drilling Project, Alpine Fault, Gaunt Creek, New Zealand, *GNS Science Report*, *2011/48*, 70.

Sutherland, R., et al. (2015), Deep Fault Drilling Project (DFDP), Alpine Fault boreholes DFDP-2A and DFDP-2B technical completion report, *GNS Science Report, 2015/50*, 269.

Templeton, E. L., and J. R. Rice (2008), Off-fault plasticity and earthquake rupture dynamics: 1. Dry materials or neglect of fluid pressure changes, *Journal of Geophysical Research-Solid Earth*, *113*(B9).

Townend, J. (1999), Heat flow through the West Coast, South Island, New Zealand, *New Zealand Journal of Geology and Geophysics, 42*(1), 21-31.

Townend, J., and M. D. Zoback (2000), How faulting keeps the crust strong, *Geology*, *28*(5), 399-402.

Townend, J., R. Sutherland, and V. G. Toy (2009), Deep Fault Drilling Project—Alpine Fault, New Zealand, *Scientific Drilling*, *8*, 75-82.

Townend, J., R. Sutherland, V. G. Toy, J. D. Eccles, C. Boulton, S. C. Cox, and D. McNamara (2013), Late-interseismic state of a continental plate-bounding fault: Petrophysical results from DFDP-1 wireline logging and core analysis, Alpine Fault, New Zealand, *Geochemistry, Geophysics, Geosystems*, *14*(9), 3801-3820.

Toy, V. G., D. J. Prior, R. J. Norris, A. F. Cooper, and M. Walrond (2012), Relationships between kinematic indicators and strain during syn-deformational exhumation of an oblique slip, transpressive, plate boundary shear zone: The Alpine Fault, New Zealand, *Earth and Planetary Science Letters*, *333*, 282-292.

Toy, V. G., C. J. Boulton, R. Sutherland, J. Townend, R. J. Norris, T. A. Little, D. J. Prior, E. Mariani, D. R. Faulkner, and C. D. Menzies (2015), Fault rock lithologies and architecture of the central Alpine fault, New Zealand, revealed by DFDP-1 drilling, *Lithosphere*, *7*(2), 155-173.

Toy, V. G., et al. (2017), Bedrock geology of the DFDP-2 drill-site, *New Zealand Journal of Geology and Geophysics, in press*, doi: 10.1080/00288306.2017.1375533.

Tullis, T. E., et al. (2007), Group report: rheology of fault rocks and their surroundings, in *Tectonic faults: agents of change on a dynamic earth*, edited by M. R. Handy, G. Hirth and N. Hovius, pp. 183–204, The MIT Press, Cambridge, MA.

Upton, P., and R. Sutherland (2014), High permeability and low temperature correlates with proximity to brittle failure within mountains at an active tectonic boundary, Manapouri tunnel, Fiordland, New Zealand, *Earth and Planetary Science Letters*, *389*, 176-187.

Upton, P., B. R. Song, and P. O. Koons (2017), Topographic control on shallow fault structure and strain partitioning near Whataroa, New Zealand demonstrates weak Alpine Fault, *New Zealand Journal of Geology and Geophysics*, 1-8, doi: 10.1080/00288306.2017.1397706.

Vry, J., R. Powell, K. M. Golden, and K. Petersen (2010), The role of exhumation in metamorphic dehydration and fluid production, *Nature Geoscience*, *3*(1), 31-35.

Wech, A. G., C. M. Boese, T. A. Stern, and J. Townend (2012), Tectonic tremor and deep slow slip on the Alpine Fault, *Geophysical Research Letters*, *39*(10).

Wech, A. G., A. F. Sheehan, C. M. Boese, J. Townend, T. A. Stern, and J. A. Collins (2013), Tectonic tremor recorded by ocean bottom seismometers, *Seismological Research Letters*, *84*(5), 752-758.

Williams, J. N., V. G. Toy, S. A. F. Smith, and C. Boulton (2017a), Fracturing, fluid-rock interaction and mineralisation during the seismic cycle along the Alpine Fault, *Journal of Structural Geology*, *103*, 151-166.

Williams, J. N., V. G. Toy, C. Massiot, D. D. McNamara, and T. Wang (2016), Damaged beyond repair? Characterising the damage zone of a fault late in its interseismic cycle, the Alpine Fault, New Zealand, *Journal of Structural Geology*, *90*, 76-94.

Williams, J. N., V. G. Toy, C. Massiot, D. D. McNamara, S. A. F. Smith, and S. Mills (2017b), Controls on fault zone structure and brittle fracturing in the foliated hanging-wall of the Alpine Fault, *Solid Earth Discuss.*, *2017*, 1-49.

Xu, S., Y. Ben-Zion, J.-P. Ampuero, and V. Lyakhovsky (2015), Dynamic Ruptures on a Frictional Interface with Off-Fault Brittle Damage: Feedback Mechanisms and Effects on Slip and Near-Fault Motion, *Pure and Applied Geophysics*, *172*(5), 1243-1267.

Zhang, H., and C. H. Thurber (2003), Double-difference tomography: The method and its application to the Hayward Fault, California, *Bulletin of the Seismological Society of America*, *93*(5), 1875-1889.

Figure 1.

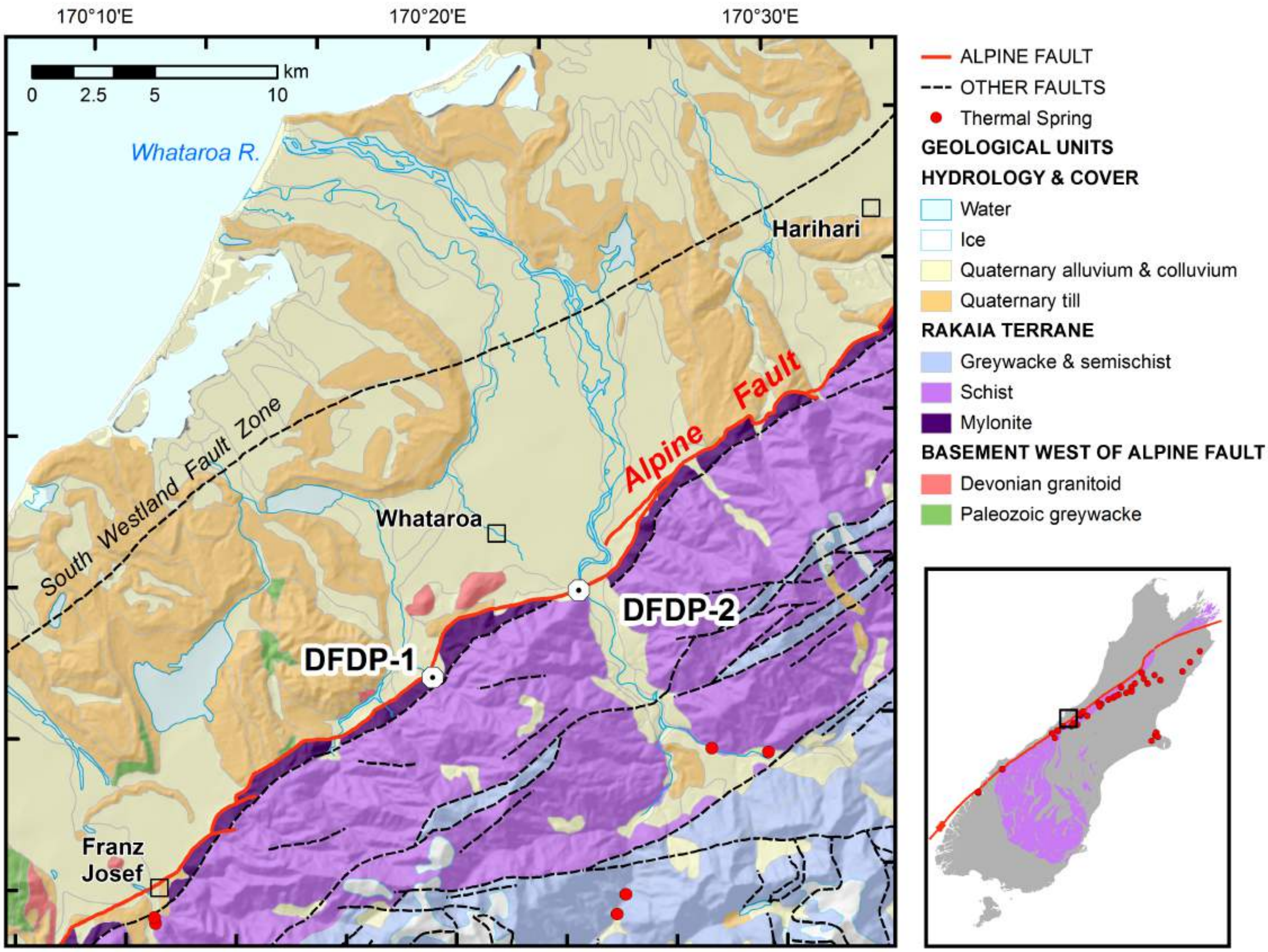
170°10'E
170°20'E
170°30'E
43°10'S
43°20'S
km
0 2.5 5 10
Whataroa R.
South Westland Fault Zone
Harihari
Alpine Fault
Whataroa
DFDP-1
DFDP-2
Franz Josef
ALPINE FAULT
OTHER FAULTS
Thermal Spring
GEOLOGICAL UNITS
HYDROLOGY & COVER
Water
Ice
Quaternary alluvium & colluvium
Quaternary till
RAKAIA TERRANE
Greywacke & semischist
Schist
Mylonite
BASEMENT WEST OF ALPINE FAULT
Devonian granitoid
Paleozoic greywacke

Figure 2.

Geology
Phase 1
Phase 2
Gravel <1ka
Gravel 12 ka
Sandy silt
Silt
Silt with gravel or boulders c. 19 ka (diamict)
Foliated schist
Foliated schist proto mylonite
Fabric dip 45-55°
Mylonite
100
200
300
400
500
600
700
800
893 m
Dual-rotary-air advance casing 16"
Rotary mud open-hole 14"
Dual-rotary-mud advance casing 12"
Dual-rotary-mud advance casing 10"
Drill 8.5" 215 mm
Casing PWT 5.5" 140 mm OD 127 mm ID
Annulus cemented with fibre optic cable behind casing in BQ pipe
Seismometer in cased hole
Cement below 400 m
Casing break at 436 m

Figure 3.

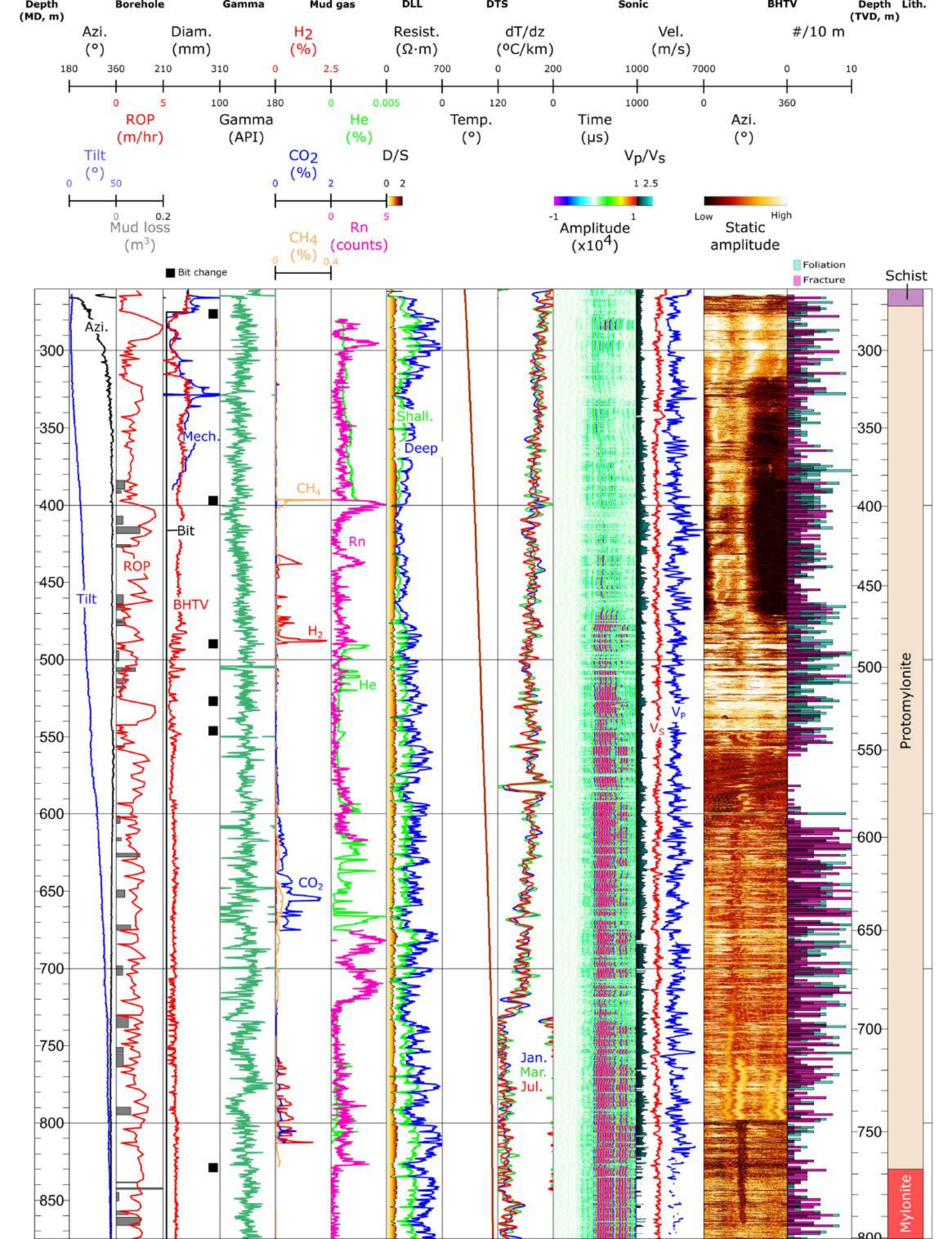

Depth (MD, m)
Borehole
Gamma
Mud gas
DLL
DTS
Sonic
BHTV
Depth (TVD, m)
Lith.
Azi. (°)
Diam. (mm)
H_2 (%)
Resist. (Ω·m)
dT/dz (°C/km)
Vel. (m/s)
#/10 m
ROP (m/hr)
Gamma (API)
He (%)
Temp. (°)
Time (μs)
Azi. (°)
Tilt (°)
CO_2 (%)
D/S
V_p/V_s
Mud loss (m^3)
CH_4 (%)
Rn (counts)
Amplitude ($\times 10^4$)
Static amplitude
Low
High
Bit change
Foliation
Fracture
Schist
Protomylonite
Mylonite
Azi.
Tilt
ROP
BHTV
Mech.
Bit
CH_4
H_2
CO_2
Rn
He
Shall.
Deep
Jan.
Mar.
Jul.
V_s
V_p

Figure 4.

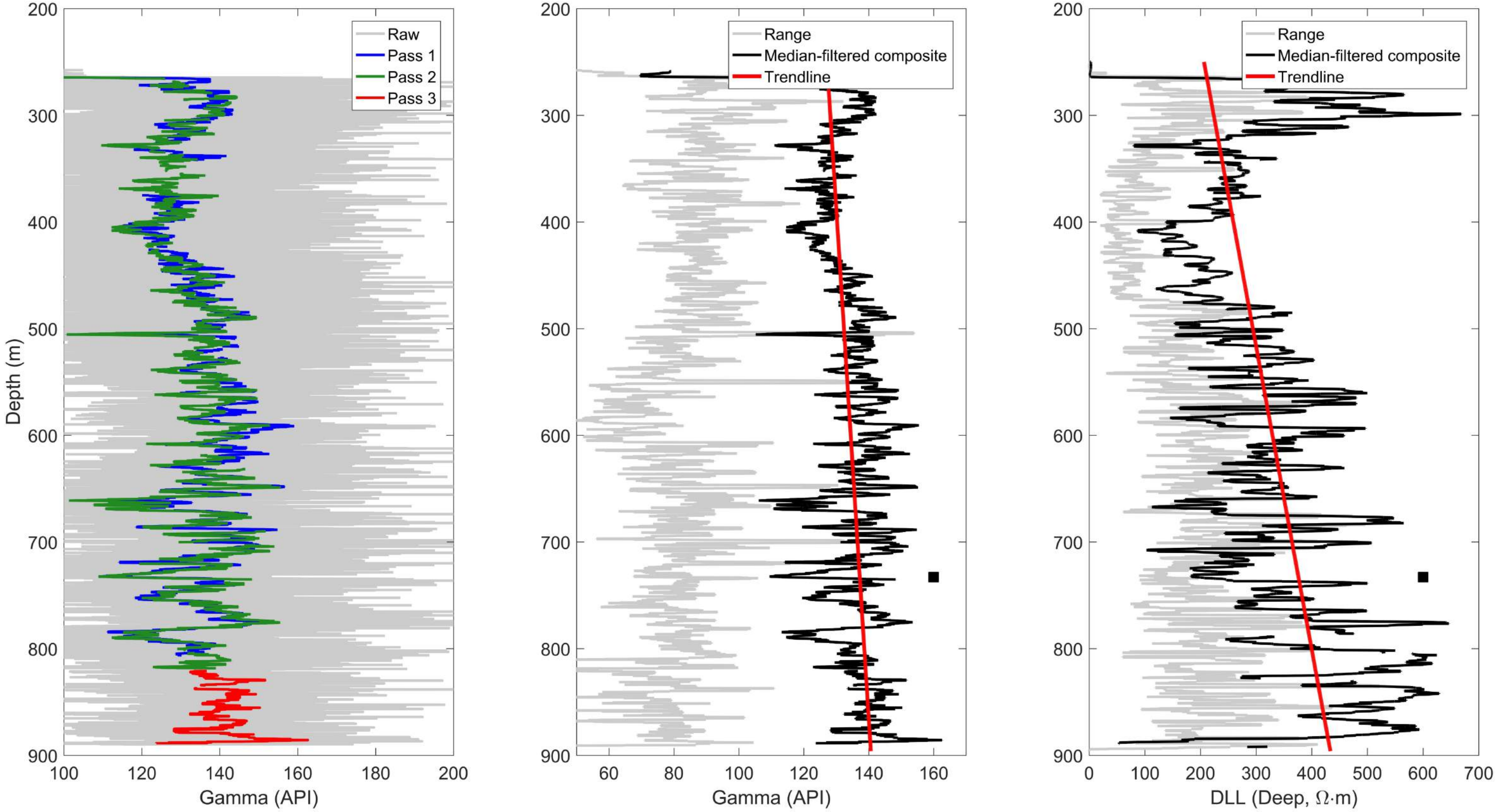

Raw
Pass 1
Pass 2
Pass 3
Depth (m)
Gamma (API)
Range
Median-filtered composite
Trendline
Gamma (API)
Range
Median-filtered composite
Trendline
DLL (Deep, Ω·m)

Figure 5.

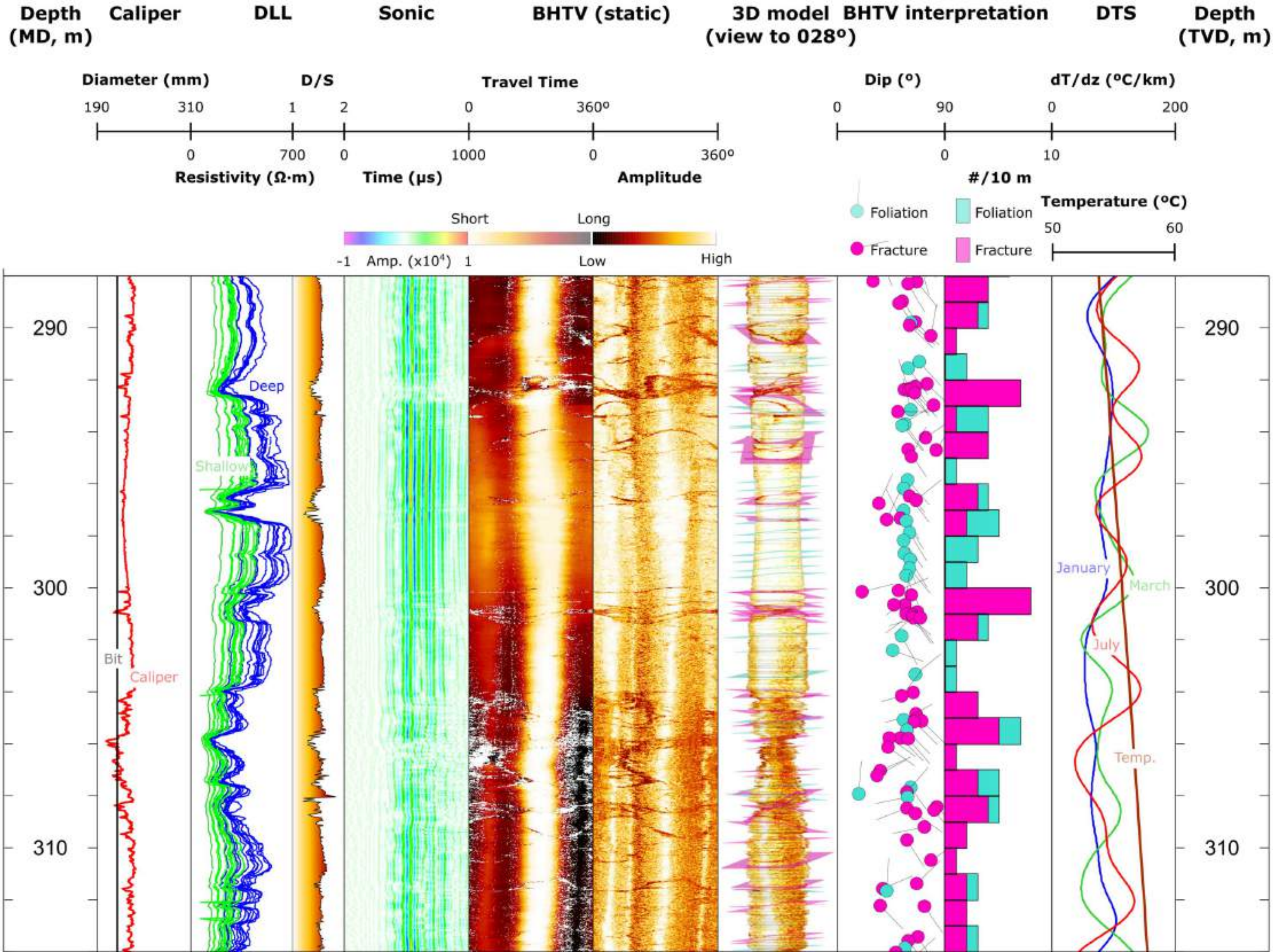

Depth (MD, m)
Caliper
DLL
Sonic
BHTV (static)
3D model (view to 028º)
BHTV interpretation
DTS
Depth (TVD, m)
Diameter (mm)
190 310
0 700
Resistivity (Ω·m)
D/S
1 2
Travel Time
0 360º
0 1000
Time (μs)
0 360º
Amplitude
Short Long
-1 Amp. (x10^4) 1
Low High
Dip (º)
0 90
#/10 m
0 10
dT/dz (ºC/km)
0 200
Foliation
Fracture
Foliation
Fracture
Temperature (ºC)
50 60
290
300
310
Deep
Shallow
Bit
Caliper
January
March
July
Temp.

Figure 6.

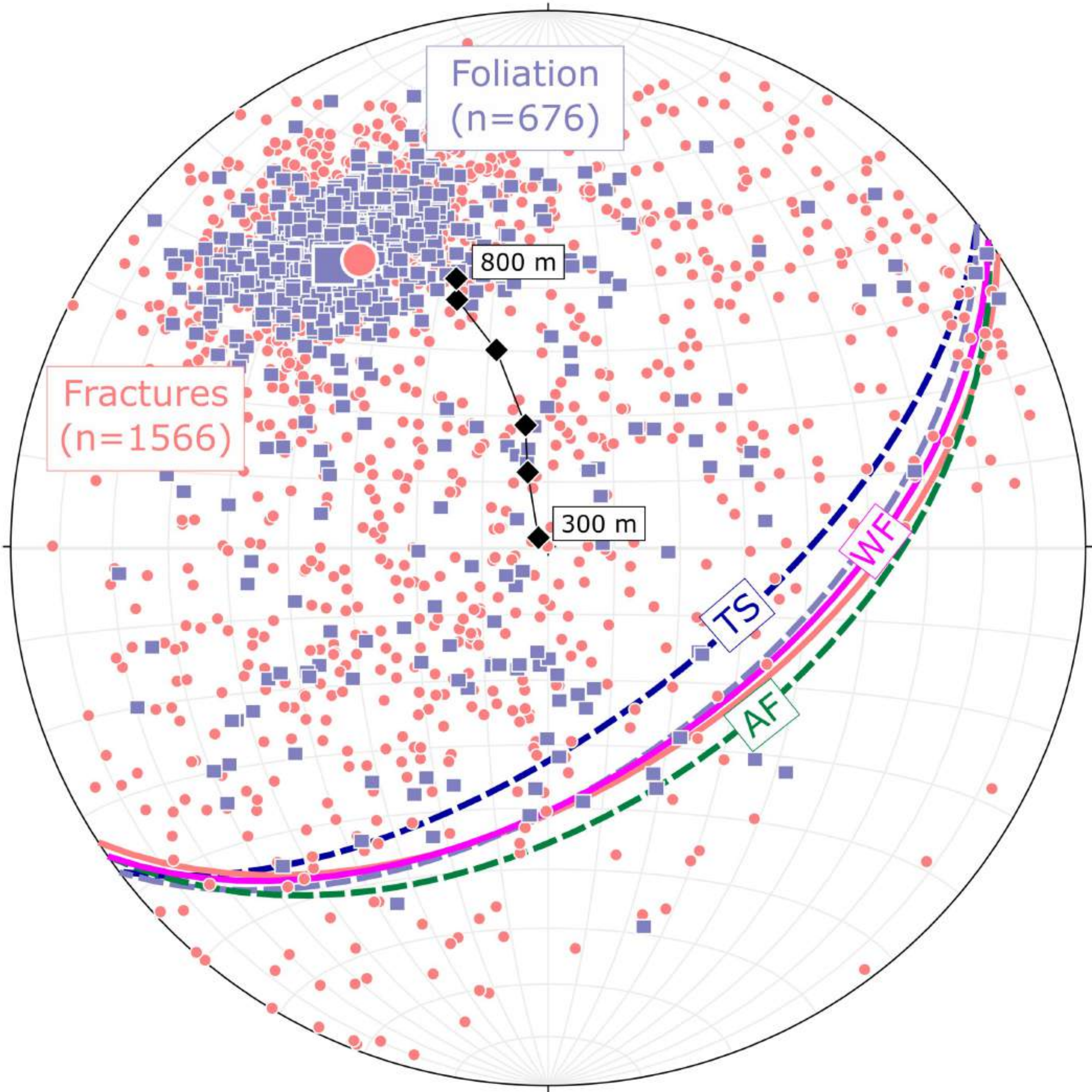
Foliation
(n=676)
Fractures
(n=1566)
800 m
300 m
TS
WF
AF

Figure 7.

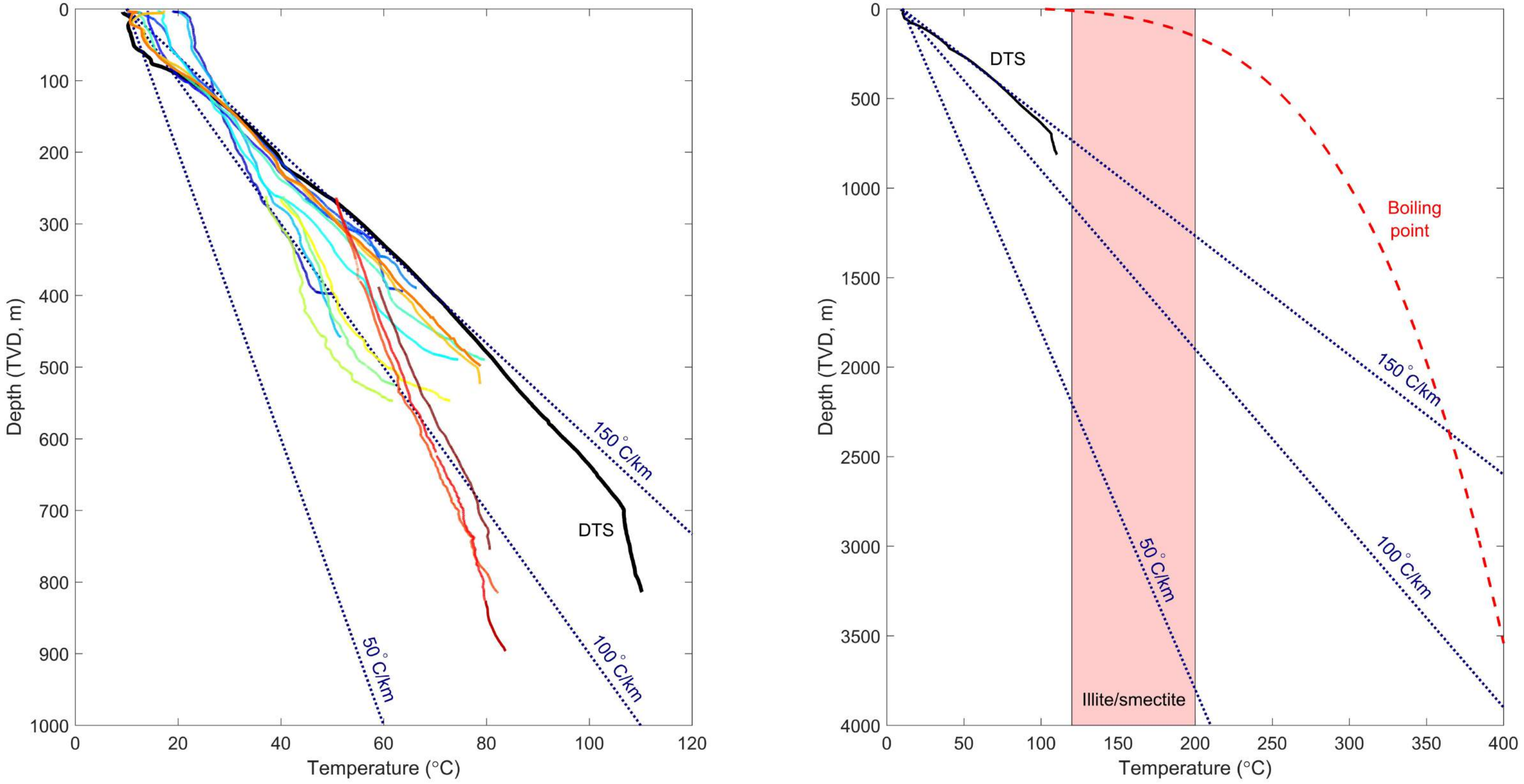

Depth (TVD, m)
Temperature (°C)
150 °C/km
100 °C/km
50 °C/km
DTS
Boiling point
Illite/smectite

Figure 8.

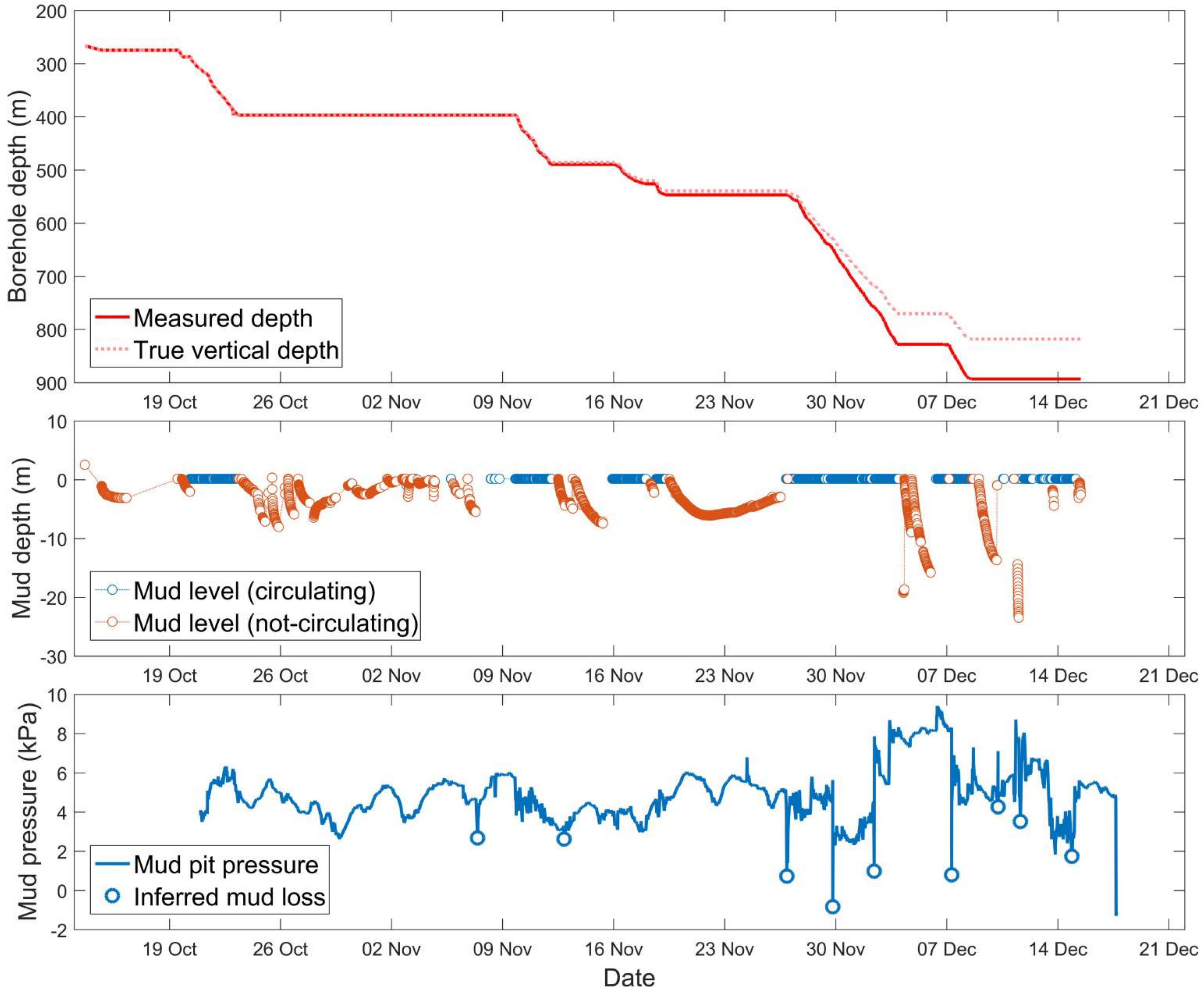
Borehole depth (m)
Measured depth
True vertical depth
Mud depth (m)
Mud level (circulating)
Mud level (not-circulating)
Mud pressure (kPa)
Mud pit pressure
Inferred mud loss
19 Oct
26 Oct
02 Nov
09 Nov
16 Nov
23 Nov
30 Nov
07 Dec
14 Dec
21 Dec
Date

Figure 9.

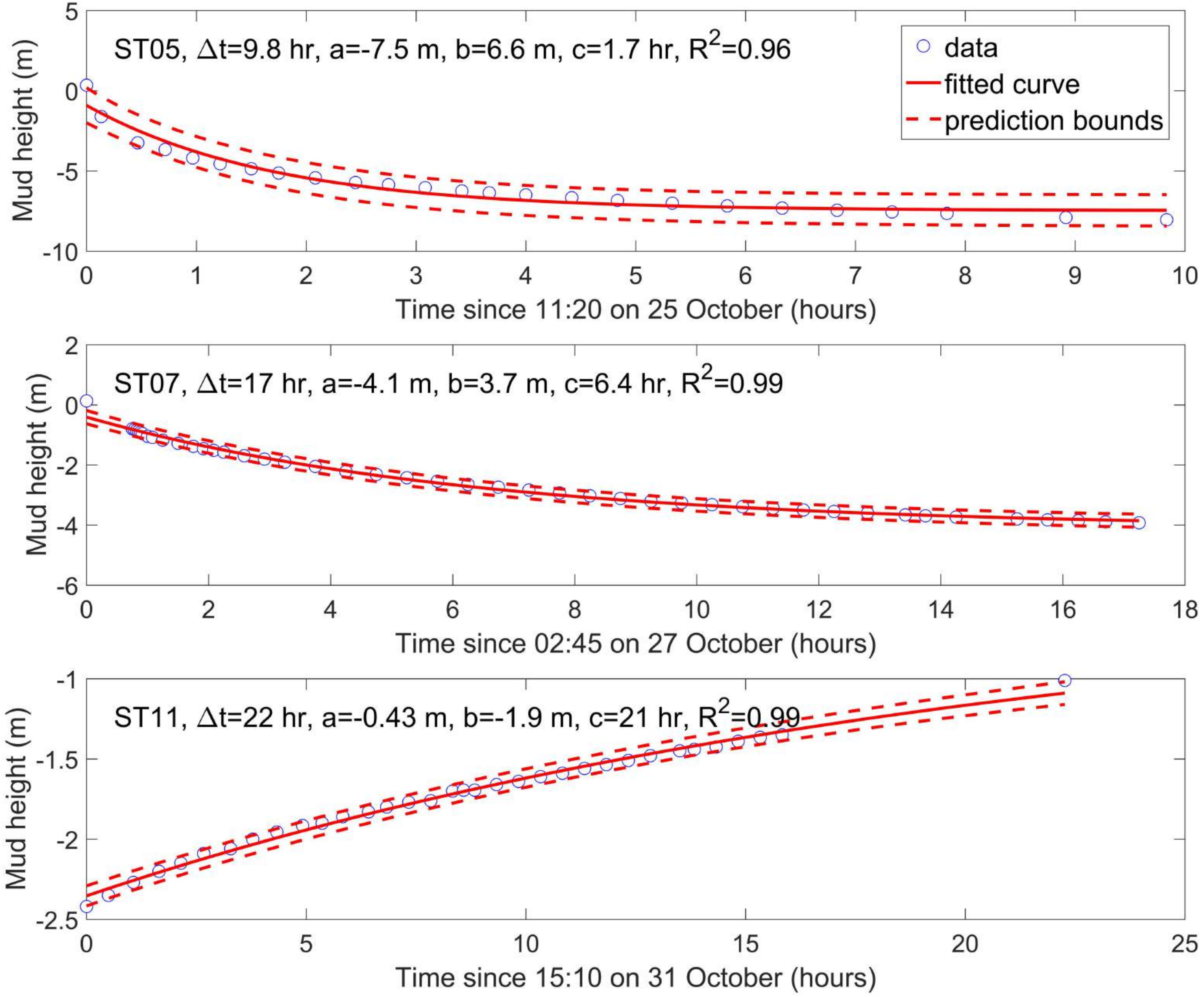
ST05, Δt=9.8 hr, a=-7.5 m, b=6.6 m, c=1.7 hr, R2=0.96
data
fitted curve
prediction bounds
Mud height (m)
Time since 11:20 on 25 October (hours)
ST07, Δt=17 hr, a=-4.1 m, b=3.7 m, c=6.4 hr, R2=0.99
Mud height (m)
Time since 02:45 on 27 October (hours)
ST11, Δt=22 hr, a=-0.43 m, b=-1.9 m, c=21 hr, R2=0.99
Mud height (m)
Time since 15:10 on 31 October (hours)

Figure 10.

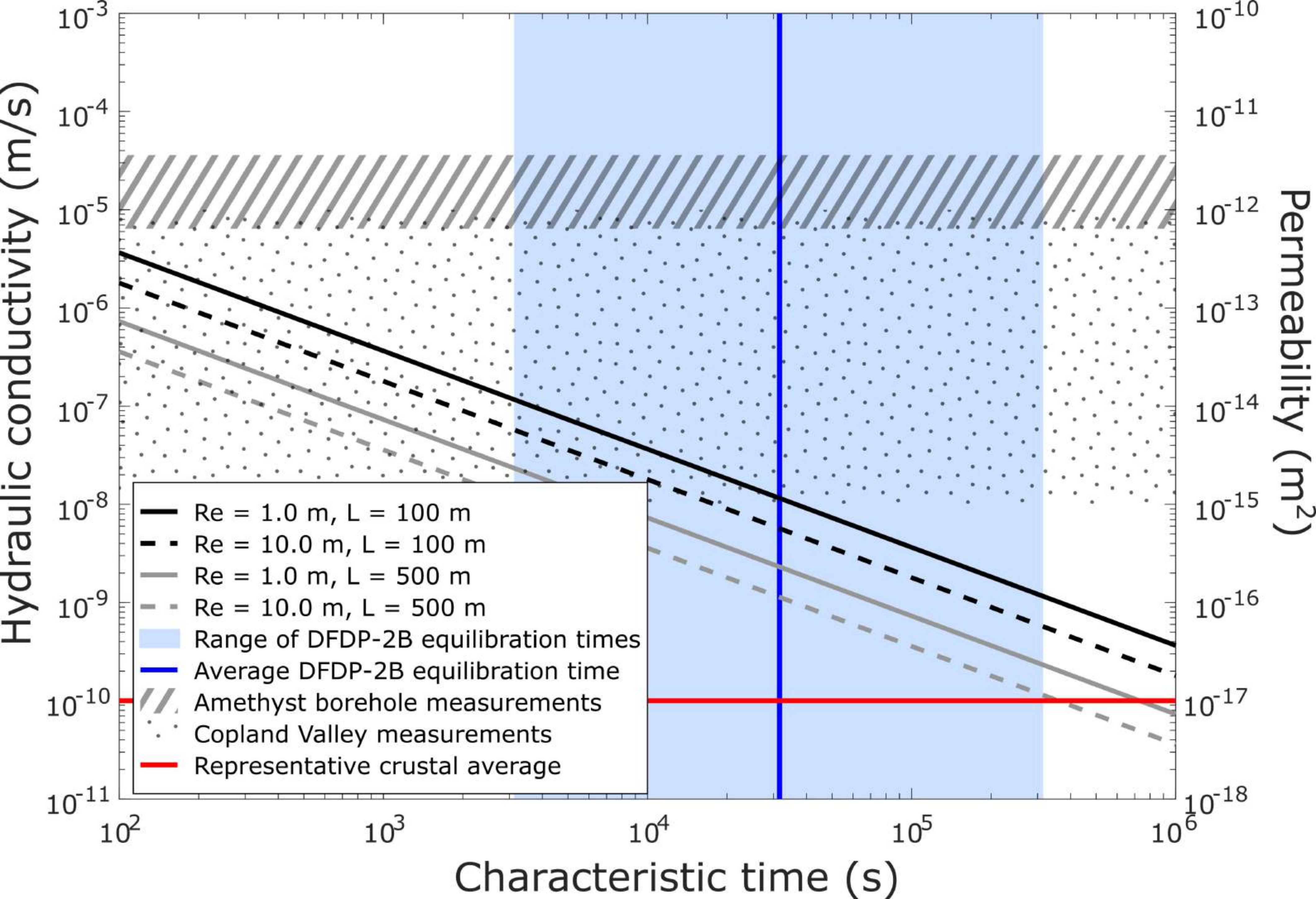

Hydraulic conductivity (m/s)
Permeability (m^2)
Characteristic time (s)
10^{-3}
10^{-4}
10^{-5}
10^{-6}
10^{-7}
10^{-8}
10^{-9}
10^{-10}
10^{-11}
10^{-10}
10^{-11}
10^{-12}
10^{-13}
10^{-14}
10^{-15}
10^{-16}
10^{-17}
10^{-18}
10^{2}
10^{3}
10^{4}
10^{5}
10^{6}
Re = 1.0 m, L = 100 m
Re = 10.0 m, L = 100 m
Re = 1.0 m, L = 500 m
Re = 10.0 m, L = 500 m
Range of DFDP-2B equilibration times
Average DFDP-2B equilibration time
Amethyst borehole measurements
Copland Valley measurements
Representative crustal average

Figure 11.

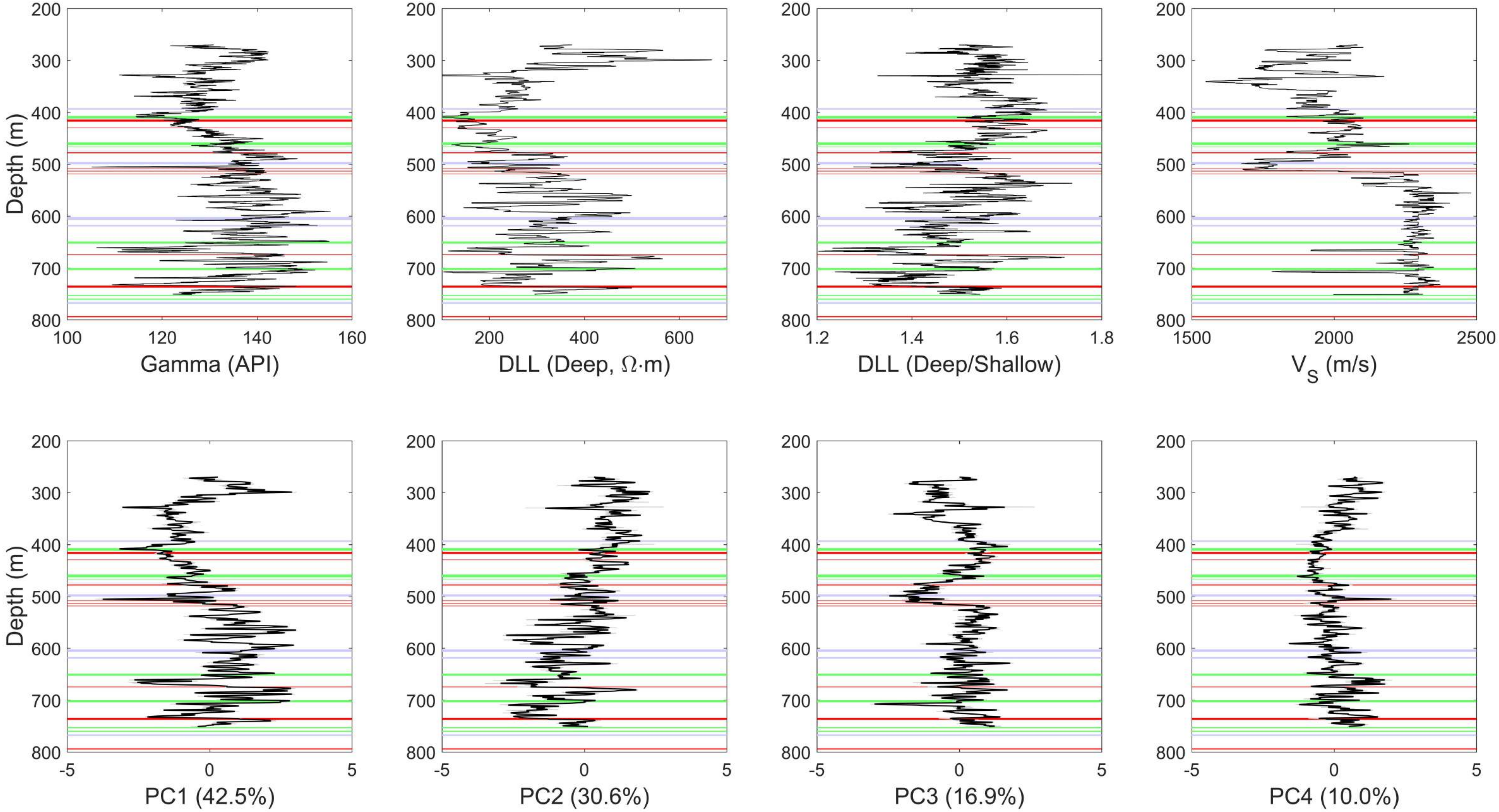

Depth (m)
Gamma (API)
DLL (Deep, Ω·m)
DLL (Deep/Shallow)
V_S (m/s)
PC1 (42.5%)
PC2 (30.6%)
PC3 (16.9%)
PC4 (10.0%)

Figure 12.

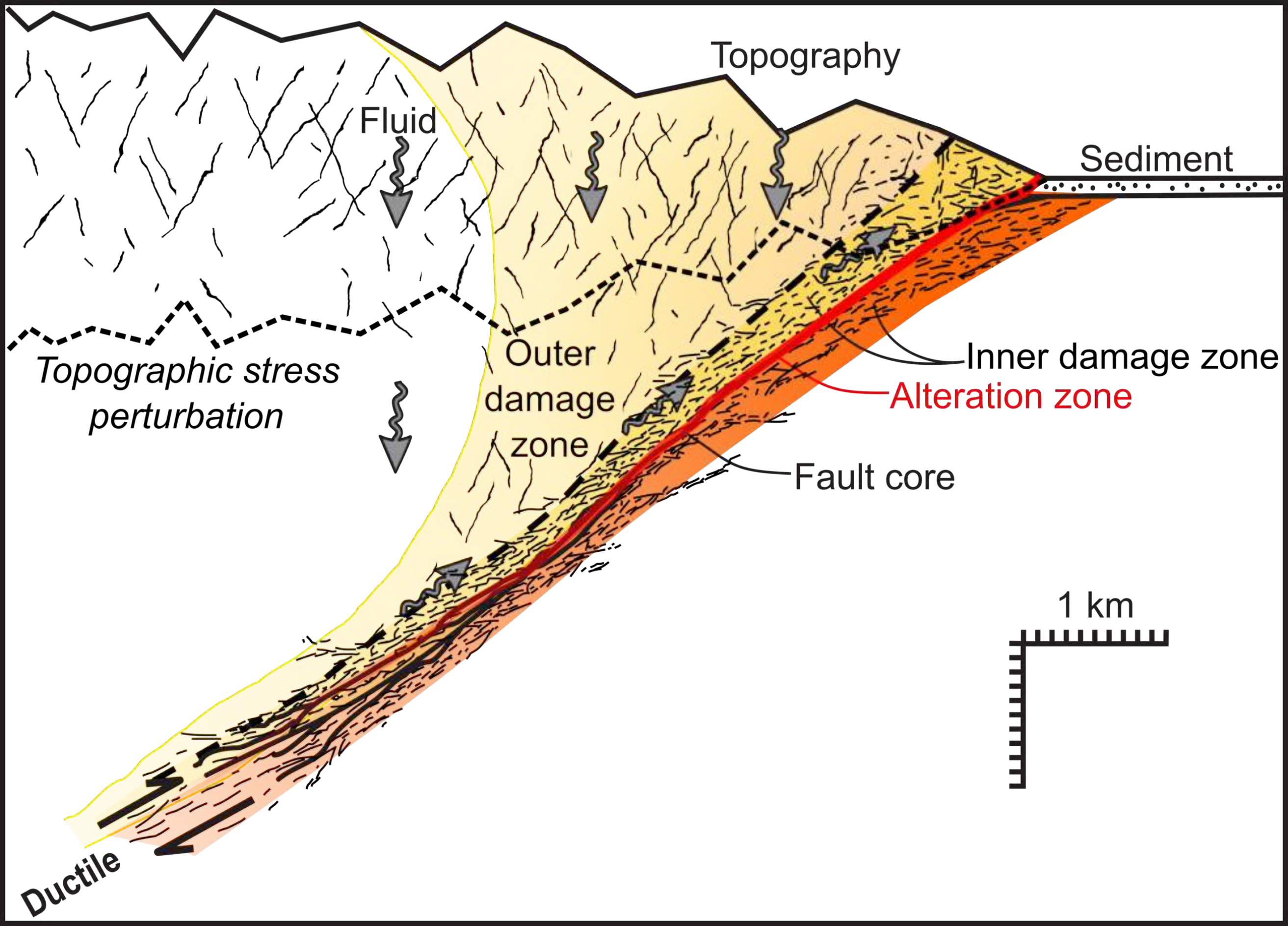
Topography
Fluid
Sediment
Topographic stress perturbation
Outer damage zone
Inner damage zone
Alteration zone
Fault core
1 km
Ductile